Microwave-Driven Hexagonal to Monoclinic Transition in $BiPO_4$: An In-depth Experimental Investigation and First-Principles Study

Ana C. M. Tello[†, ‡], Marcelo Assis[†], Ricardo Menasce[†], Amanda F. Gouveia[†], Vinicius Teodoro[†], Natalia Jacomaci[§], Maria A. Zaghete[§], Juan Andrés[¥], Gilmar E. Marques[£], Marcio D. Teodoro[£], Albérico B. F. da Silva ‡, Jefferson Bettini[¤], Elson Longo[†]*

[†]CDMF, LIEC, Chemistry Department of the Federal University of São Carlos - (UFSCar), P.O. Box 676, 13565-905 São Carlos, SP, Brazil.

[‡]Instituto de Química de São Carlos, Universidade de São Paulo, São Carlos - SP, P.O. Box 780, 13566-590, SP, Brazil.

[§]CDMF, LIEC, Chemistry Institute of the Paulista State University - UNESP, P.O. Box 1680, 14801903, Araraquara, SP Brazil.

[¥]Department of Physical and Analytical Chemistry, University Jaume I (UJI), Castelló 12071, Spain.

[£]Physics Department, Federal University of São Carlos - (UFSCar), P.O. Box 676, 13565-905 São Carlos, SP, Brazil.

[g]Brazilian Nanotechnology National Laboratory (LNNano), Rua Giuseppe Maximo Scolfa no 10000, Campinas BR-13083100, SP, Brazil.

KEYWORDS: $BiPO_4$, polymorphism, first principle calculations, photoluminescence emissions, photocatalyts, morphology control.

ABSTRACT: Present theoretical and experimental work provides an in-depth understanding of the morphological, structural, electronic, and optical properties of hexagonal and monoclinic polymorphs of $BiPO_4$. Herein, we demonstrate how microwave irradiation induces the transformation of the hexagonal to a monoclinic phase one in a short period of time and thus, the photocatalytic performance of $BiPO_4$. To complement and rationalize the experimental results, first-principle calculations have been performed within the framework of the density functional theory. This was aimed at obtaining the geometric, energetic and structural parameters as well as vibrational frequencies; further, electronic properties (band structure diagram and density of states) of the bulk and the corresponding surfaces of both hexagonal and monoclinic surfaces of $BiPO_4$ were also acquired. A detailed characterization of the low vibrational modes of both hexagonal and monoclinic polymorphs is key in explaining the irreversible phase transformation from hexagonal to monoclinic. Based on the calculated values of the surface energies, a map of the available morphologies of both phases was obtained by using the Wulff construction and compared with the observed SEM images. The $BiPO_4$ crystals obtained after 16-32 min of microwave irradiation provided excellent photodegradation of Rhodamine B under visible light irradiation. This enhancement was found to be related to the surface energy and the types of clusters formed on the exposed surfaces of the morphology. These findings provide details of the

hexagonal to monoclinic phase transition in $BiPO_4$ during microwave irradiation; further, the results will assist in designing electronic devices with higher efficiency and reliability.

INTRODUCTION

Bismuth phosphate ($BiPO_4$) is a promising photocatalyst that is activated by visible light. It demonstrates double the activity of TiO_2 (P25, Degussa) for the degradation of organic dyes under ultraviolet (UV) light[1]; further, it exhibits enhanced photocatalytic activity toward NO purification[2,3]. $BiPO_4$ presents hexagonal and monoclinic polymorphs that comprise both distorted tetrahedral [PO_4] and octahedral [BiO_6] clusters, which are the primary building blocks of the polymorph. However, both polymorphs present different photocatalytic activity, which is highly dependent on the structure, electronic properties, morphology of these phases; consequently, it is reliant its exposed surfaces as well[2, 4-7]. In particular, Fu et al.[8] have reported that the monoclinic phase of $BiPO_4$ is the preferred crystalline structure for the degradation of benzene; this is due to the structural distortion of the tetrahedral [PO_4] cluster and the large band gap structure[9-11]. The preparation of $BiPO_4$ polymorphs (hexagonal and monoclinic) has been successfully carried out by several methods. The pure hexagonal phase of $BiPO_4$ has already been obtained by conventional hydrothermal[12], microwave assisted hydrothermal (MAH)[13], and sonochemical[14,15] methods under mild synthesis conditions. In turn, the pure monoclinic phase is usually obtained by the conventional hydrothermal method, which exhibits long synthesis periods (2h-96h) and temperatures up to 200 °C[1, 2, 16-18]. Wang et al. also observed the formation of the monoclinic phase using the MAH method, but with the addition of an ionic liquid in the reaction medium[19]. Few studies in the literature also show the conversion of the hexagonal phase to the monoclinic phase by the hydrothermal method[12] through the incorporation of compression[20] or doping processes[21, 22]. Chen et al. observed complete conversion by employing the time frame

of 1 to 3h at a temperature of 200 °C[23]. Further, Zhu et al. required up to 12h of synthesis at 150 °C to complete the conversion of the hexagonal phase to monoclinic[24]. In these studies, it is evident that complete conversion from one phase to the other was directly proportional to the temperature employed during the synthesis.

Among the different solution-based synthesis techniques, microwave irradiation has garnered a widespread scope of remarkably new opportunities to explore its applications in the area of material science. Microwave irradiation in a suitable solvent has been widely applied for the rapid synthesis of inorganic solids at relatively lower temperatures within a short reaction time (within minutes) as compared to conventional heating[25-27]; further, it has received special attention owing to its interesting advantages, which include rapid, uniform, and selective heating, reduced processing costs, better production quality, and the possibility of modifying the phase stability and the morphology beyond thermodynamic equilibrium. This has led to the fabrication of new materials that are technologically important such as meta-stable phases, which are not accessible by conventional methods[28-30]. Further, microwave heating is an inexpensive, facile, and relatively fast method for the preparation of crystalline samples, which exhibit unique or enhanced properties; further, these can be used to fabricate products with narrow particle size distribution and increased phase purity[30-34]. However, microwave-specific thermal effects and microwave non-thermal effects are still poorly understood, especially during synthesis procedures[35].

Recently, the structures and energetics of four low index stoichiometric surfaces ((001), (010), (011), and (100)) of monoclinic monazite $BiPO_4$ have been studied from a theoretical point of view by using density functional theory (DFT) calculations[36]. Fun et al.[37] showed that monoclinic $BiPO_4$ exhibits a dendritic morphology, and performs well as a photocatalyst for the degradation

process of benzene; this is due to the presence of highly energetic (002), (012), and (031) surfaces and the oxygen vacancies (). However, the role of the exposed surfaces and morphology on the photocatalytic activity are still unrevealed. To the best of our knowledge, reports on the direct visualization of the transition process between hexagonal and monoclinic phases have been very limited; in addition, deep insight into the surface-dependent photocatalytic activity of both hexagonal and monoclinic polymorphs of materials based on $BiPO_4$ has not been yet carried out.

An attractive alternative, but yet underexplored strategy to gain control over phase transition is provided by regulating the microwave irradiation while keeping all other parameters constants. Therefore, understanding the phase transition process, at the atomic scale, can allow an efficient phase-controlled synthesis that leads to crystal structure with improved properties and thus may have new materials with potential for various technological applications. Inspired by the above considerations, we report a novel study on the gradual transformation of hexagonal $BiPO_4$ to the monoclinic polymorph upon microwave irradiation without the addition of any surfactants and templates; the $BiPO_4$ microcrystals initially exhibit a hexagonal structure and are obtained by a simple co-precipitation (CP) method. Our principal aim was to understand the fine effects of the microwave irradiation on the morphology and photoluminescence (PL) emissions of the as-synthesized $BiPO_4$ crystals, and to investigate the role of the electronic structure on their photocatalytic activity. Herein, we elucidate these points by performing a detailed theoretical and experimental study on the photocatalytic activity in the degradation process of Rhodamine B (RhB) under visible irradiation. The synthesized materials were characterized by X-ray diffraction (XRD) with Rietveld refinement, scanning electron microscopy (SEM), and micro-Raman spectroscopy. Moreover, their optical properties were investigated by using ultraviolet-

visible (UV-vis) spectroscopy and PL measurements at room temperature. First-principles theoretical calculations within the framework of density functional theory (DFT) were employed to obtain atomic level information of the geometry and electronic structure, local bonding, band structure, density of states (DOS), and vibrational frequencies. The morphologies of the as-synthesized samples are obtained by SEM images, and their corresponding transformations are rationalized; this is achieved by using the Wulff construction and altering the relative values of the surface energies of the different surfaces. The effect of time on the formation of hexagonal and monoclinic phases and on their structural, morphological, and absorption properties was investigated. Furthermore, by combining the results obtained from first-principle calculations and experimental measurements, the crystal structure, electronic properties, and surface energies characteristics of $BiPO_4$ were analysed; this was aimed at achieving deep insights into the morphology characteristics, optical properties, and photocatalytic activity toward RhB. The accurate prediction of the structure, stability, electronic structure, and morphologies of $BiPO_4$ is an essential prerequisite for tuning their electronic properties and functions.

This paper contains three more sections. The next section is the experimental section where the synthesis, characterization, computational details, and model systems are elucidated. In section three, the results are presented and discussed. The main conclusions are summarized in the fourth section.

EXPERIMENTAL

Synthesis. The $BiPO_4$ samples were synthesized by the CP method at 30 °C in an aqueous medium. The precursors used were $Bi(NO_3)_3 \cdot 5H_2O$ (98%, Aldrich) and $(NH_4)_2HPO_4$ (98%, Alfa-Aesar). Further, 1 x 10^{-3} mol of $Bi(NO_3)_3 \cdot 5H_2O$ and 1 x 10^{-3} mol of $(NH_4)_2HPO_4$ were dissolved

separately in 30 ml of deionized water. The $Bi(NO_3)_3 \cdot 5H_2O$ solution was poured into the $(NH_4)_2HPO_4$ solution and stirred for 20 min. The suspensions obtained were transferred to a Teflon autoclave, sealed, and placed in the MAH system (2.45 GHz, maximum power of 800 W). The reaction mixtures were heated to 160 °C for 2, 4, 8, 16 and 32 min. Subsequently, the precipitate was decanted and washed several times with distilled water and dried at 60 °C for 12 hours.

Characterization. The $BiPO_4$ samples were structurally characterized by XRD using a D/Max-2500PC diffractometer (Rigaku,) with Cu Kα radiation (λ = 1.5406 Å) in the 2θ range of 10 - 110° and a scanning speed of $1°min^{-1}$ in the Rietveld routine. The Rietveld refinement method was employed to understand the structural differences and the phase composition of the $BiPO_4$. In this analysis, the refined parameters were: the scale factor, background, shift in the lattice constants, profile half-width parameters (u, v, w), isotropic thermal parameters, lattice parameters, strain anisotropy factor, preferred orientation, and atomic functional positions. Further, micro-Raman spectra were recorded using the iHR550 spectrometer (Horiba Jobin-Yvon) coupled to a Silicon CCD detector and an argon-ion laser (Melles Griot, USA), which operated at 514.5 nm with a maximum power of 200 mW; moreover, a fiber optic microscope was also employed. UV-Vis diffuse reflectance measurements were obtained using a Varian Cary spectrometer model 5G in the diffuse reflectance mode, with a wavelength range of 200 to 800 nm and a scan speed of 600 nm min^{-1}. Photoluminescence measurements were performed at room temperature by using a 355 nm laser (Cobolt/Zouk) as an excitation source, which was focused on a 200 μm spot at a constant power of 5 mW. The luminescence signal was dispersed by a 19.3 cm spectrometer (Andor/Kymera) and detected by a Silicon Charged Coupled Device

(Andor/IdusBU2).The morphologies, textures, and sizes of the samples were observed with a SEM, which operated at 10 kV (Supra 35-VP, Carl Zeiss).

Photocatalysis. To perform the photocatalysis experiments, 50 mL of RhB (95%, Malinkrodt) solution $1x10^{-5}$ $molL^{-1}$, was mixed with 50 mg of $BiPO_4$. The mixture, consisting of the dye and photocatalyst, was irradiated in a dark box using 6 lamps (PHILIPS TL-D, 15 W). Before the illumination, the suspensions were sonicated for 15 min in an ultrasonic bath (42 kHz, model 1510, Branson, USA) to allow saturated absorption of RhB onto the catalyst. Subsequently, the dispersion containing the catalyst and the dye was transferred to a vessel inside the photo-reactor, with the temperature maintained at 20°C via a thermostatic bath and vigorous stirring in the dark for 30 min. After this process, the solution is exposed to light, and 2 mL aliquots were withdrawn at 0, 2, 4, 6, 8, 10, 15, 20, 30, 40, 50 and 60 min, each aliquot of the suspension was removed and placed in centrifuge tube, which was then spun at 10000 rpm for 10 min to separate the solid catalyst from the liquid phase. Finally, the kinetics of the dye photodegradation process were monitored in a commercial cuvette via UV-Vis spectroscopy (JASCO V-660) at 554 nm.

Computational Details and Model Systems. Hexagonal ($P3_121$) and monoclinic (P121/n1) phases of the $BiPO_4$ have been studied by using periodic DFT calculations with the B3LYP hybrid functional[38] using the CRYSTAL14 code[39]. Bi atom was described by using the effective core potential (ECP) modified from Hay and Wadt[40] while the P and O atoms were described from all-electrons pob_TZVP_2012basis sets[41], as obtained from the Crystal web site.

The accuracy of the Coulomb and exchange integral calculations (TOLINTEG) was controlled by five parameters set to 10^{-7}, 10^{-7}, 10^{-7}, 10^{-7} and 10^{-14}, the reciprocal space was considering in a 6x6 mesh (SHRINK) corresponding to 6 independent k-points in the Brillouin zone according to

the Pack-Monkhorst method[42]. The band structure and DOS were obtained for 100 *k*-points along the appropriate high symmetry paths of the adequate Brillouin zone.

The equilibrium morphology of a crystal was calculated based on the classic Wulff construction[43], by minimizing the total surface energy () at a fixed volume, providing a simple relationship between the of the plane (hkl) and its distance in the normal direction from the center of the crystallite[44]. is defined as the energy per unit area required to form the surface relative to the bulk and is calculated according to equation:

Eq.4

Where is the energy of the relaxed slab, is the number of $BiPO_4$ units in the slab and is the energy of the bulk, and A is the surface area. The factor 2 in the denominator represents the upper and lower surfaces of the slab. The position of all atoms of the slab was relaxed.

Slab models were employed to simulate the surfaces of low index for both $BiPO_4$ hexagonal (with Miller indices (hkl):, , ,, , ,), and monoclinic (with Miller indices (hkl): , ,, , , , ,)) were used in the calculations. The thickness of each slab model was optimized until convergence of cutting energy was achieved. The calculations were carried out using slabs with atomic layers and periodic boundaries as the bulk in *a* and *b* directions while *c* is a non-periodic direction with a sufficient number of layers to minimize the interaction between the upper and lower surfaces of the slab. The number of layers in the slabs for the hexagonal phase is: 51 for , 36 for , 54 for , 50 for , 80 for , 90 for and 106 for the thickness value corresponding to the number of layer to each surface is: 1.796 nm, 1.856 nm, 1.615, 1.746, 1.409, 1.433 and 1.540 nm, respectively. The number of layers in the slab for the monoclinic phase was selected as: 72 for , , , , and) surfaces and 60 for and surfaces, the thickness value corresponding to the number of layer to each surface is: 1.748, 1.937, 1.713, 1.950, 1.467, 1.400, 1.905 and 1.885 nm, respectively.

Furthermore, in order to reduce the calculation cost and keep charge neutrality, the stoichiometry of the slab model is maintained as in the bulk model.

The procedure to obtain the complete set of morphologies, which are based on the Wulff construction and the surface energy, has been previously presented by our research group[45]; further, it was successfully used to obtain the morphology of materials, including $PbMoO_4$, α-Ag_2MoO_4, $BaMoO_4$, $BaWO_4$, $CaWO_4$, Ag_3PO_4, Ag_2CrO_4 and $LaVO_4$[46-53].

In addition, the broken bonding density (), which is defined as the number of bonds broken per unit cell area when a surface is created can be calculated by using Eq. 5[54,55]:

Eq. 5

Where is the number of broken bonds per unit cell area on a specific surface and A is the area unit of the surface. From the values derived from , we can predict the order of surface stability as we know that higher values are related to larger quantities of defects present on the surface[56].

The polyhedron energy () was calculated with Eq. 6 and energy profiles were constructed, allowing us to associate the ideal morphology with the final experimental morphology.

Eq. 6

Where is the percentage contribution of the surface area to the total area of polyhedron () and is the surface energy[57].

RESULTS AND DISCUSSION

X-Ray Diffraction. Figure 1 shows the XRD patterns of the $BiPO_4$ samples obtained by the CP method and also of those subjected to microwave irradiation at different times. XRD analysis were performed to demonstrate the order/disorder transition at long-range, or to determine the periodicity and arrangement of the crystalline lattice. All samples exhibit well defined diffraction peaks, indicating a good degree of structural order at long-range in the crystalline lattice.

<INSERT FIGURE 1>

The samples synthesized by the CP method and irradiated by microwave at 2 and 4 min correspond to $BiPO_4$ with hexagonal structure and space group $P3_121$; this was in accordance with card no. 67986[58] in the Inorganic Crystal Structure Database (ICSD) with lattice parameters a = 6.9885 Å, c = 6.4867 Å, α = β = 90°, and γ = 120°. For the samples irradiated by microwave at 8 and 16 min, the formation of the monoclinic phase of $BiPO_4$, belonging to the space group P121n/1, was observed in addition to the hexagonal phase of $BiPO_4$; this was in accordance with card no. 67987[58] in the ICSD. The lattice parameters of the monoclinic phase are *a* = 6.7626 Å, *b* = 6.9516 Å, *c* = 6.4822 Å, α = γ = 90 °, and β = 103.7°. For the sample obtained after 32 min, only the monoclinic phase was observed. Thus, by increasing the time of exposure of the microwave irradiation, a complete conversion occurs from the hexagonal to the monoclinic phase. A schematic 3D representation of the structure hexagonal and monoclinic of $BiPO_4$ is depicted in Figure 2, theoretical and experimental values of the P–O and Bi–O distances and O–P–O and O–Bi–O angles are presented in Tables SI-1 and Table SI-2 (in the Supporting Information, SI).

<INSERT FIGURE 2>

The parameters obtained in the Rietveld refinements of $BiPO_4$ powders are shown in Table SI-3 and Table SI-4, and their structural results are presented in Figure 3, in which the statistic fitting parameters (R_{wp} and GOF see Table SI-3, Supporting Information) indicate that the quality of structural refinement data is acceptable (Figure SI-1). The calculated equilibrium lattice parameters of the two phases of $BiPO_4$ are also shown in Table SI-4.

An analysis of the results presented in Table SI-1 and Table SI-2 renders slight differences between the calculated and experimental data of bond distances and angles, which can be

attributed to differing synthesis conditions. Following the proposal of Xu et al.[36], and Zhu et al.[59] we assumed that both polymorphs can be described by [BiO_6] and [PO_4] clusters.

Thus, more specifically, the [BiO_6] clusters correspond to a distorted octahedron in the hexagonal phase with the Bi–O bond length in the range of 2.368 Å to 2.558 Å (see Table SI-3) and a distorted oblique triangular prism in the monoclinic phase with the bond length of Bi–O in the range of 2.326 Å to 2.523 Å (see Table SI-4). Both [BiO_6] and [PO_4] clusters are more distorted in the monoclinic polymorph with respect to the hexagonal one. The larger variety of Bi-O and P-O bonds in monoclinic $BiPO_4$ is responsible for the significant structural distortions at both [BiO_6] and [PO_4] clusters. Such behaviour is primarily observed in the [PO_4] tetrahedron, and has assumed to be responsible for the higher photocatalytic activity of monoclinic polymorph when compared with the hexagonal phase of $BiPO_4$[60, 61].

It is observed in Figure SI-2A that a partial conversion between hexagonal and monoclinic phases occurs after 8 min of microwave irradiation, while pure monoclinic polymorph is obtained at 32 min. In order to understand how the conversion between phases occurs, an analysis of the lattice parameters was performed from the Rietveld refinement data. It is observed that during the first 4 min of microwave irradiation, there is a reduction in the *a* and *c* lattice parameters of the hexagonal structure; this indicates a contraction of the crystalline cell (Figure SI-2B and C). The phase transformation process from hexagonal to monoclinic requires energy, which was supplied by the dipolar polarization of the water solvent and ionic conduction from the dissolved precursors in the reaction medium; this led to the rapid heating of the system that enhanced the energy transfer process during the microwave irradiation[62]. The energy provided to the system is used to induce a rearrangement in the positions of atoms in the unit cell, i.e. the Bi and P cations in the [BiO_6] and [PO_4] clusters, respectively, undergo changes in

both Bi–O and P–O bond lengths as well as O–Bi–O and O–P–O bond angles. The sample obtained after 4 min of microwave irradiation has sufficient energy to induce structural distortions at these clusters, which are essentially precursors of the monoclinic structure. After 8 min of microwave irradiation, an expansion in the lattice parameters of the hexagonal phase was observed, until it was completely converted into a monoclinic polymorph. When the monoclinic phase is formed, the hexagonal unit cell relaxes and expansion of the crystal lattice can be detected. Otherwise, when both phases coexist, a decrease in the values of the lattice parameters (*a*, *b* and *c*) can be observed (see Figures SI-2D, E and F) for the monoclinic phase. However, when the monoclinic phase is obtained, there is an increase in the values of these lattice parameters.

Micro-Raman Spectroscopy. Micro-Raman spectroscopy (Figure 3) is an important technique for understanding the effects of structural order/disorder transition at short-range in crystalline solids. The Raman spectrum, for a crystal without defects, should comprise of lines corresponding with central points in the allowed zone, which is in accordance with the rules of selection. According to group theory analysis, the allowed representation for each of the corresponding Wyckoff positions of the hexagonal structure of $BiPO_4$ in the symmetry group indicates 26 active Raman modes corresponding to the decomposition at the point $\Gamma = (8A_1 + 18E_1)$[10]. For the monoclinic structure of $BiPO_4$, which belongs to the group of symmetry , 36 corresponding Raman active modes of decomposition of the point $\Gamma = (18A_g + 18\ B_g)$ are obtained[10, 63]. Micro-Raman spectra of the samples synthesized in 4 min exhibit only active modes that are associated with the hexagonal phase; for samples synthesized in 8 min, the appearance of the active modes of the monoclinic phase can be observed. For the sample synthesized after 32 min, only the modes referring to the monoclinic structure were observed in Raman as well as in

XRD spectra; this indicates the complete conversion of the hexagonal structure to a monoclinic one.

<INSERT FIGURE 3>

For the hexagonal structure of the $BiPO_4$, 11 modes are observed. There are three modes located at 89.7, 138.6 and 198.9 cm^{-1}, which are assigned to the symmetric bending of the O-Bi-O moiety[10, 13, 14, 64]. The three modes observed at 397.4, 439.4, and 466.6 cm^{-1} are related to bending vibrations (ν_2) of the [PO_4] clusters[10, 13, 14, 64]. The Raman modes observed at 544.6 and 584.6 cm^{-1} are attributed to asymmetric stretching vibrations (ν_4) of the [PO_4] cluster[10, 13, 14, 64]. The most intense modes, observed at 964.0 and 1053.2 cm^{-1}, are associated to symmetric (ν_1)[10, 13, 14, 64]. For the monoclinic structure of the $BiPO_4$, 13 modes are observed. The modes located at 91.7, 122.9, 163.0, 225.7, and 272.3 cm^{-1} are associated with the stretching of the Bi-O bonds[6, 65]. The modes observed at 379.5 and 399.5 cm^{-1} correspond to the bending vibrations (ν_2) of [PO_4] clusters, while the modes at 450.9, 548.9, and 589.1 cm^{-1} correspond to the bending vibrations (ν_4) of [PO_4] clusters[6, 65]. The highest intensity modes at 961.7 and 1030.9 cm^{-1} are related to the symmetric (ν_1) and asymmetric (ν_3) stretching modes of the cluster [PO_4], respectively[6, 65]. Further, it was observed that samples that are subjected to synthesis for up to 4 min comprise only the modes that are associated with the hexagonal phase; meanwhile, for the synthesis above 8 min, the samples display active modes for the monoclinic phase. For the sample synthesized with 32 min, as well as in XRD spectrum, only the modes associated with the monoclinic structure are observed; this indicates a complete conversion of the hexagonal structure to a monoclinic one.

Figure SI-3 displays a comparison between the experimental and calculated values of the Raman modes of both hexagonal (Figure SI-3A) and monoclinic (Figure SI-3B) structures. Both

experimental and theoretical results are in accordance with results previously reported in the literature (see Table SI-5 and SI-6)[10], which indicate that our computational methodology and optimized unit cells provide a good representation of the two polymorphs of $BiPO_4$.

Proposed Mechanism. Based on the analysis of the above results and, in particular, the characteristics of both $[BiO_6]$ and $[PO_4]$ clusters along the transformation from hexagonal to monoclinic structure, we propose the following mechanism for the formation of both polymorphs and their subsequent irradiation transformation.

$Bi(NO_3)_{3(aq)}$, $(NH_4)_2NaPO_{4(aq)}$ are the precursors of the Bi and P cations, respectively, along the CP synthesis method and their environments control the geometry and electronic properties of both $[BiO_6]$ and $[PO_4]$ clusters, as final constituents of both hexagonal and monoclinic polymorphs of $BiPO_4$.

First, $Bi(NO_3)_3$ was dissolved in water, giving the hexahydrate complex of Eq. 7, while the phosphate source was dissolved in water to form $(PO_4)^{3-}$ (Eq. 8), both processes can be described as a chemical equilibrium:

Eq. 7

Eq. 8

On the other hand, $(Bi(OH_2)_6)^{3+}$ and $(PO_4)^{3-}$ can be considered as the precursors of $[BiO_6]$ and $[PO_4]$ clusters in the solid state, respectively. In the next step both clusters are capable to form the hexagonal $BiPO_4$ phase and posterior microwave irradiation converts this to monoclinic $BiPO_4$ polymorph, as it is represented in Figure SI-4.

Along the CP method used to obtain $BiPO_4$, the formation of the hexagonal polymorph, with presence of $[BiO_6]$ and $[PO_4]$ clusters with minor structural distortions, is favored due to the low temperature and mild conditions. When this polymorph is irradiated by microwaves, a

combination of recrystallization/dissolution processes are promoted and a symmetrical breaking process takes place, in which more structurally distorted [BiO_6] and [PO_4] clusters appear, enhancing formation of monoclinic polymorph. As reported in the literature, the phase transition requires only a small rotation of the polyhedron for a suitable symmetrical arrangement[38, 40, 66], therefore, it is expected that a coherent coupling between the microwave field radiation with low frequency modes of the system, translational and rotational modes, can induce the structural changes at both [BiO_6] and [PO_4] clusters.

The theoretical vibrational spectrum present five low frequency modes (<100 cm^{-1}) in hexagonal $BiPO_4$ at wavelength of 66.57, 70.68, 77.7, 85.6 and 97.45 cm^{-1}. By the analysis of the animation of these vibrational modes using CRYSPLOT, we can visualize the atomic movements in each wavelength. The phase transition hexagonal to monoclinic is then attributed to the combination of these five modes, i.e. the mode at 66.57 cm^{-1} is responsible of the displacement of the Bi cation, the vibrational mode at 70.67 cm^{-1} (Figure 4) is linked to the rotation of the O anions at [BiO_6] cluster, while the vibrational mode at 77.7 cm^{-1} is assigned to the rotation of the O anions at [PO_4] cluster.

<INSERT FIGURE 4>

These findings seem to indicate that the energetic *stimuli*, provided by the microwave irradiation, is capable to active these low vibrational modes to enhance the phase transformation, from the hexagonal to the monoclinic polymorph. At the local coordination, the distorted octahedron [BiO_6], at the hexagonal phase, undergoes a structural rearrangement to distorted oblique triangular prism [BiO_6] in the monoclinic polymorph. This monoclinic $BiPO_4$ phase presents low vibrational modes at 71.3 and 78.28 cm^{-1}, but the corresponding movements are not associated to the transformation from monoclinic to hexagonal polymorph. Therefore, these

results seem to indicate that the phase transition from hexagonal to monoclinic, induced by microwave irradiation, corresponds to an irreversible process.

A note of caution is mandatory here, our previous analysis is based on the low vibrational modes of the hexagonal phase to explain the initial vibrational modes responsible for the phase transition, but a correct explanation need to be obtained by characterizing transition state, and in particular their transition vector, i.e, their unique imaginary vibration mode that controls this phase transition.

Photoluminescence (PL) Emissions. PL measurements were also performed in order to investigate the influence of structural ordering of defects of $BiPO_4$ samples. Figure 5A shows the PL emissions under a UV laser excitation (λ = 355 nm). All samples show PL emission in the range of the visible spectrum with a broad-band profile, which is characteristic of multi-phonon processes, ruled by the presence of high density of electronic levels within the band gap[67-70]. In order to verify the whole PL emission, an analysis by *Commission Internationale de l´Éclairage* (CIE) coordinates was performed by SpectraLux software[71]. Figure 5B shows the CIE chromaticity diagram for PL spectra of all samples. Although there are slight differences in the color shades, all samples presented emissions in the green region of the visible spectrum.

<INSERT FIGURE 5>

The PL emissions were deconvoluted using the Voigt function, to quantify the contributions of each defect to the PL emission, as shown in Figure SI-5. There were three components centered at 470, 535 and 607 nm, corresponding to blue, green and orange of visible spectrum, respectively. It is known that each emitted color derives from an associated type of defect acting as a luminescent center within the material[72-74]. In the broad-band PL model, defects that emit

higher energy in the visible spectrum, as blue and violet, are assigned to structural defects, i.e. angular distortions at the [BiO_6] and [PO_4] clusters, which leads to larger changes in the electronic levels of the material, termed shallow defects. The emission of green and orange colors is associated to the presence , presenting a range of energies due to the contribution of charge transfer between neutral (), mono-ionized () and doubly-ionized () states of oxygen vacancies, also called as deep defects[75-77].

Table SI-7 presents the contribution of the components of the PL spectra. We observed that the blue contribution which corresponds to structural defects raised in the initial 4 min of synthesis, decreased as function of time of exposure of microwave irradiation. the sample obtained at 4 min of microwave irradiation presents higher structural distortions compared to other samples when studied by Rietveld refinement, and a larger contraction of both *a* and *c* lattice parameters can be sensed. These structural strains induce angular distortions on the clusters that compose the unit cell. To gain a deeper insight on the nature of structural and electron changes the green and orange components in the emission (correspond to the presence of) were summed and considered as deep defects in Table SI-7. An analysis of the results indicates that while blue coloration increases, the deep defects contribution decreases. It is believed that the oxygen vacancies originate from the variations in the lengths of Bi/P-O bonds and that this is a sign of increase in the structural distortions at both [BiO_6] and [PO_4] clusters, and subsequently growth in the lattice parameters of the unit cell. It can also be noted that the 8 min sample shows an expansion of both *a* and *c* lattice parameters of the unit cell, we also see increase in the contribution of deep defects to the PL emissions. In the 16 min sample, a slight increase in the blue contribution as observed in comparison to the 8 min sample, indicating a decrease in deep defects. These changes can also be confirmed by the results of Rietveld refinement due to the

slight decrease of the lattice parameter c of the hexagonal unit cell. This contraction arises possibly due to the abrupt increase in the monoclinic phase content compared with the 8 min sample, which can generate a mismatch in the interface between both phases. These results indicate that the strain in the lattice parameter *c* axis had a large contribution to the defects that act as luminescent centers for $BiPO_4$ samples. The sample irradiated for 32 min presents an increase in the deep contribution versus 16 min, which can also be confirmed by the enlargement of the of *a*, *b* and *c* lattice parameters of the monoclinic unit cell. This behavior can be considered as a signature of the presence of both oxygen vacancies and distorted $[BiO_6]$ and $[PO_4]$ clusters. Therefore, we are capable to connect the results of the PL emissions and Rietveld refinement, i.e. larger structural distortions, involving Bi–O and P–O distances, and O–Bi–O and O–P–O bond angles increases the contribution to blue emission. Moreover, with an increase of oxygen vacancies, a larger expansion of the unit cell takes place with a concomitant increase of green and orange emissions.

Electronic properties of the bulk. The band structures were obtained for 100 *k*-points along the appropriate high symmetry paths of the adequate Brillouin zone, and the diagrams of states were calculated for analysis of the corresponding electronic structures. Figure SI-6 and SI-7 present the band structure, the total DOS projected in all atoms of the bulk and of the surfaces for both polymorphism and also the partial DOS (PDOS) projected in the *s* and *p* (p_x, p_y and p_z) orbitals in the bulk for the two $BiPO_4$ structures._As can be observed in Figure SI-6, for the $BiPO_4$ hexagonal phase, the top of the valence band (VB) is located between K and H points of Brillouin zone and the bottom of conduction band (CB) and also located at the same region of the k-space close to the H point. The calculated band gap value is 5.40 eV corresponding an indirect transition while the experimental value in this work was 4.60 eV.

In the case of the monoclinic phase (Figure SI-7), the top of the VB is located mainly between D and C points and the bottom of the CB is located at the region between E and Γ points. The band gap calculated is 4.60 eV corresponding to an indirect transition and the experimental value report in this work was 3.80 eV. Band gap experimental values between 3.5–4.6 eV have been reported, which depend on the size of the particle and the method of synthesis[59, 66, 78].

Based on the analyses of DOS and PDOS, it can be deduced that both hexagonal and monoclinic $BiPO_4$, the VB is predominantly formed by the contribution of the O atoms, with a small contribution of P and Bi atoms. In this VB an overlap of O orbitals with the Bi orbitals occur. The CB is formed mainly by the orbitals from the Bi atoms with a small contribution of the orbitals of the O atoms and orbitals of the P atoms. These results are in accordance with other calculations reported in the literature[59, 66, 78].

Scanning Electron Microscopy (SEM) Analysis. The SEM images of the morphologies of the obtained $BiPO_4$ samples are displayed in Figure 6. It is clearly seen that the synthesized $BiPO_4$ suffers change in its shape with the increase of the microwave irradiation. The $BiPO_4$ obtained by CP method (hexagonal phase) has the shape of needles that agglomerate to form larger deformed rods (Figures 6A). When the $BiPO_4$ is subjected to microwave irradiation at 2, 4 and 8 min (Figures 6B-D), the hexagonal phase is predominantly observed, and there is an increase in the size of the needles that form the rod microstructure, and well-defined hexagonal rods appear. When the monoclinic phase is predominant, at 16 and 32 min of microwave irradiation, (Figures 6E-F), the microstructures change into beveled tetragonal rods. This effect is due to the continuous dissolution/recrystallization processes that occur in $BiPO_4$ induced by the microwave irradiation, and thus, structural changes take place at short, medium and long-distance, as discussed above.

<INSERT FIGURE 6>

Structure of $BiPO_4$ surfaces. The key to investigating the photocatalysis on model surfaces is a detailed knowledge of bare surface structures. In the absence of this information, mechanistic interpretation of photochemical reactions can only be speculative. Sometimes, it may simply be incorrect. Through direct tracking the evolution of crystal surfaces using a combination of SEM images and first-principle calculations on model $BiPO_4$ surfaces for both hexagonal and polymorphs is discussed. Then the details of our photocatalysis on the model surfaces are presented, attempting to probe the Bi–O and/or P–O bond cleavages with formation of under-coordinated $[BiO_6]$ and $[PO_4]$ clusters at the exposed surfaces step by step. Figure 7 displays the slab models of the , , ,, , , and surfaces of the hexagonal $BiPO_4$, while in Figure 8, the slab models of the (, , ,, , , and surfaces for the monoclinic $BiPO_4$. At the top of each surface model, Figures 7 and 8 can be observed different kinds of under-coordinated cluster for the Bi and P cations when compared with the bulk, which are generated because of direct cutting of the crystal along the surface in the slab construction where different bonds have been broken.

<INSERT FIGURE 7>

<INSERT FIGURE 8>

Thus, for the hexagonal phase the and , surfaces, present only one kind of under-coordinated cluster , it is worth noting that all studied surfaces present this kind of under-coordinated cluster, with exception for the surface which present only an under-coordinated cluster . In surface, under-coordinated cluster of and is present. The surface is formed by , and clusters. The most unstable surfaces, and , are formed by under-coordinated and clusters which are common to both surfaces, while on the surface, the clusters appear, and in surface, and clusters are found.

In the case of the monoclinic phase, under-coordinated Bi cation, and and clusters, can be observed, and under-coordinated and clusters centered around the P cation can be sensed. More specifically, , , and surfaces are characterized for present only the under- coordinated cluster. In the case of surface can be observed , clusters as well as cluster. On the other hand, surface presents four kind of under-coordinated cluster: , , and . The surface displays the and clusters, while surface, is formed for the under-coordinated and clusters, and it is the only surface that present clusters.

By comparison of the calculated values shown in Table SI-8 and Table SI-9. It is possible to establish an order of thermodynamic stability for these surfaces, thus, to $BiPO_4$ hexagonal the following order of decreasing stability is established: > > > > > > while for $BiPO_4$ monoclinic of decreasing order of stability is: > >> > > > > .

With the reported in Table SI-8 and SI-9 and employing the Wullf construction method, the ideal crystal morphology for each polymorph was constructed, as well as the complete map of available morphologies by changing the values of the (increases or decrease) of the different surfaces. Figures 9 and 10 (top) show the available morphologies of both hexagonal and monoclinic polymorphs of $BiPO_4$. Experimental SEM images are also included for comparison purposes with the calculated morphologies.

<INSERT FIGURE 9>

<INSERT FIGURE 10>

The ideal morphology of the hexagonal phase is characterized by a six-fold geometry (see Figure 9) that is controlled by , and surfaces. Starting from the ideal morphology and aiming to obtain a similar morphology to the experimental SEM images, which present a six-fold pyramidal geometry, the values of the surface energy for the and were decreased and the

surface energy for was increased, simultaneously. On the other hand, a similar morphology of experimental geometry can also be obtained through stabilization of the (1012) surface. However, we associated the experimental morphology with the controlled morphology for the surface, as reported by Li et al.[13] in which the HR-TEM image of an individual $BiPO_4$ nanoparticle shows the presence of plane in the hexagonal phase.

In the case of the monoclinic phase of the $BiPO_4$ (see Figure 10 (top)), the ideal morphology is controlled by , , and surfaces. The experimental morphology was simulated by means of two paths: the first from shape A and by stabilizing surface to obtain shape A1 and subsequently by stabilizing and destabilizing simultaneously, obtaining shape A2. The second path was reached stabilizing surface which is theoretically the most unstable surface and surface, simultaneously to obtain shape B1 and destabilizing surface, to obtain shape B2. We have associated our experimental morphologies with the B1 and B2 shapes. The A2 and D morphologies generated are similar to that reported by Li et al.[21]

Furthermore, the polyhedron energy () was calculated and also the energy profiles which allows to connect the ideal morphology with the final experimental morphology were constructed and are depicted in Figure 9 and 10 (bottom) for $BiPO_4$ hexagonal and monoclinic, respectively. The reaction diagram to obtain the final experimental morphologies of $BiPO_4$ hexagonal evidences a process barrier less thermodynamically favorable (Figure 9 (bottom)) while the reaction path for $BiPO_4$ monoclinic presents a minimum of energy via morphology B1 (Figure 10 (bottom)). The parameters used to calculate are reported in Table SI-10 and SI-11.

According to Table SI-8 for hexagonal $BiPO_4$ there is a correlation between the surface stability and the broken bond number (). The and surfaces have the lowest energy with similar values of = 0.44 and 0.47 Jm^{-2}, respectively, and the lowest value of the broken bond number

(=2) establishing an equal stability order for these two surfaces. The , , , , and surfaces follow a decreasing order of stability with = 0.52, 0.55, 1.06, 1.28 and 1.39 Jm^{-2}, respectively, and with = 4, 6, 8, 12, 14, respectively.

In the case of the monoclinic $BiPO_4$, Table SI-9, and surfaces have the lowest energy with similar values = 0.66 and 0.69 Jm^{-2}, respectively, with the same broken bond number = 2. The , surface with = 0.86 and 1.05 Jm^{-2}, respectively, with equal value of = 4. Additionally, , , and surfaces present decreasing order of stability from values = 1.23, 1.36, 1.74 and 2.56 Jm^{-2}, respectively, with the = 6, 8, 12, 14. Therefore, in this case, we are unable to establish a correlation between the surface stability and the broken bond number.

In relation to the electronic properties of the surfaces (Figure SI-6B and SI-7B), in both hexagonal and monoclinic phases all surfaces present an insulating band gap as the original bulk. The energy gap values for each surface are presented in Table SI-8 and SI-9 for hexagonal and monoclinic phases, respectively.

In general, on the surfaces of both polymorphs the main contributor to the VB region is the O 2*p* orbitals and P 3*p* orbital and fewer contributions from the Bi 3*s* orbitals. To the CB predominantly we observed Bi 3*p* orbitals and P 3*p* orbitals, in the and surfaces of the hexagonal phase and the and surfaces of monoclinic phase, where important contributions from P 3*p* orbitals are observed. The presence of under-coordinated clusters in the surfaces, modifies the distribution of the electron states and induce the formation of intermediate energy levels, flat bands in the band gap region. Thus, in the monoclinic phase the band gap of the surfaces decrease as the oxygen vacancies increase while in the hexagonal phase the band gap is reduced in , and surfaces due to the presence of an under-coordinated cluster of and . Oxygen vacancies also split-off in the O 2*p* orbitals in the VB observed.

Photodegradation Process. The photocatalytic activity of the $BiPO_4$ samples were tested for chromophore degradation of RhB under visible light irradiation. RhB shows a characteristic absorption peak located at 556 nm, relative to its conjugated chromophore xanthene ring, in the presence of light and $BiPO_4$ it undergoes a hypochromic absorption displacement as a result of the de-ethylation of the N,N'-diethylammonium functional groups[33]. When RhB solution was subjected to visible light irradiation without a catalyst, (photolysis test) practically no degradation was observed. The photodegradation results are shown in Figure 11A by variations of RhB concentration (C_n/C_0) as function of irradiation time, being C_n and C_0 the concentration at a time t and the initial concentration, respectively. Since most of the heterogeneous photocatalytic mechanisms for semiconductors are considered as pseudo-first order reaction due to the low initial concentration of dye and the constant concentration of catalyst, the Langmuir-Hinshelwood (L-H) model was used[79,80]:

Eq. 9

Here, k is the rate constant and t the reaction time. Therefore, if the reaction order is of pseudo-first order, the plot of $-\ln(C_n/C_0)$ as a function of irradiation time gives a straight line in which the angular coefficient is the k value. The L-H plots were performed in order to verify the reaction order and to obtain the rate constant for all samples, as shown in Figure 11B.

<INSERT FIGURE 11>

The photodegradation behavior change is observed according to the time employed at the microwave irradiation. The hexagonal phase $BiPO_4$ synthesized by the CP method has an 85% rate of RhB chromophore photodegradation. After the sample was subjected to microwave irradiation for 2, 4 and 8 min, an inhibition of photodegradation activity is observed. This happens because the surfaces employed in the electron-hole recombination process of the

hexagonal phase of $BiPO_4$ observed predominantly in these samples (2, 4 and 8 min) is different to that observed in the $BiPO_4$ sample obtained by the CP method. The surface stabilization of the obtained materials is intrinsically linked to the kinetic change in the balance of ordered and disordered [BiO_6] clusters due to microwave action. The sample obtained by CP method has no defined surfaces and may have several different types of oxygen vacancies () on its surface, both coming from Bi clusters and P clusters. When the hexagonal samples of $BiPO_4$ obtained at 2, 4 and 8 min by microwave irradiation are analyzed, we can observe the stabilization of the surfaces , which has two clusters with (), and), which has three in the clusters and . The stabilized surfaces employed in the photodegradation process cannot perform electron-hole recombination, becoming ineffective in this process. Moving from the hexagonal phase to the monoclinic phase of the $BiPO_4$, at the 16 and 32 min samples, an efficiency of 83 and 79% is observed for photodegradation respectively. This is due to the stabilization of the surfaces , which has two cluster with (), , which has two clusters with () and , which has six in the clusters , and .

Photocatalytic activity is dependent on the electron-hole recombination rate of the material. The hexagonal structure of $BiPO_4$ obtained by CP has a high degree of order/disorder, so the electron-hole recombination rate is more effective, enabling RhB photodegradation. Analyzing the structures obtained in 2, 4 and 8 min, the hexagonal phase reorganization was observed, resulting in new morphologies of $BiPO_4$. The results obtained for these samples at long-distance (XRD) correspond with an increase of material organization, creating new active sites and reducing electron-hole recombination. The transformation from hexagonal to monoclinic structure causes a structural reorganization, generating new active sites for electron-hole stabilization, making the photodegradation process of RhB effective again.

Due to these results, photocatalytic experiments using scavenger reagents were performed for the $BiPO_4$ CP and the $BiPO_4$ 32 min samples, in order to understand the photodegradation mechanism. As a control for these experiments, tert-butyl alcohol (TBA), silver nitrate (SN), p-benzoquinone (BQ), and ammonium oxalate (AO) were used as scavengers for hydroxyl radicals, electrons, superoxide radicals, and holes, respectively. Figure 11C shows the photodegradation efficiency of samples of $BiPO_4$ with and without scavengers. All the experiments for both samples, i.e. the absence of hydroxyl radicals, electrons, superoxide radicals, and holes for reactions, presented inhibited or lower photodegradation efficiency compared to the $BiPO_4$ samples without scavengers. From these results, we propose a photodegradation mechanism, as given by Figure 12, which were constructed with Kröger-Vink notation[81].

<INSERT FIGURE 12>

In Figure 16, the $BiPO_4$ surface clusters are represented for the general formula (where A = P and Bi, y = 2, 4 and 5, n = 1 and 2, to represent , and). The presents in the clusters can become and according to the movement of electrons and holes in the $BiPO_4$ surface by cluster-cluster charge transfer (I, II and II in Figure 12). Losing electrons (I and II in Figure 12), the formation of and in the clusters favors the processes that lead to oxidation of H_2O and reduction of O_2 (IV and V in Figure 12), which generate reactive oxygen species (ROS), the hydroxyl radical and the hydroperoxyl radical . This process can be observed for samples obtained by CP method and at 16 and 32 min of microwave irradiation. After ROS production, the clusters regenerate, continuing the oxidation processes (VI in Figure 12). The is generated by the reaction of the proton () with the superoxide radical [82]. Electron recovery for the formation of is not favorable

for photocatalysis oxidation processes, which probably occur for samples obtained at 2, 4 and 8 min of microwave irradiation (III and VII in Figure 12).

CONCLUSIONS

As has emerged from this work, microwave irradiation upon materials can be exploited for enhance phase transition. Here, we present a combined theoretical and experimental study dedicated to analyze the microwave-driven hexagonal to monoclinic transition in $BiPO_4$. The study has been made possible by the combination of experimental techniques (XRD with Rietveld refinement, SEM, and micro-Raman and UV-vis spectroscopies, and PL measurements) and first principle calculations, at the DFT level. We have observed the phase transition of hexagonal to monoclinic $BiPO_4$ under microwave irradiation; in addition, by analyzing the structural ad electronic differences between these polymorphs and their exposed surfaces, the highest photocatalytic activity of monoclinic $BiPO_4$ exhibited when compared with the hexagonal $BiPO_4$ is disclosed.

The main conclusions of this work can be summarized as follows:

(i) $BiPO_4$ crystals with hexagonal structure were successfully synthesized by the simple co-precipitation method and, for the first time, the effect the microwave irradiation to induce the irreversible phase transition from hexagonal into monoclinic $BiPO_4$ polymorph have been reported. Hexagonal $BiPO_4$ is unstable under microwave irradiation, spontaneously transforming to the monoclinic phase $BiPO_4$ in short time and thus, enhancing photocatalytic performance of $BiPO_4$.

(ii) The first-principles calculations performed at the DFT level provide an in-depth understanding of the electronic and structural properties of the bulk and selected surfaces of both polymorphs of $BiPO_4$, namely: hexagonal and monoclinic.

(iii) A detailed analysis of the low vibrational modes of both hexagonal and monoclinic polymorphs depicts that the movements associated with these modes are the key to explain the irreversible phase transformation of hexagonal to monoclinic, which is induced by microwave irradiation.

(iv) Present understanding suggests that structural and electronic distortions of $[PO_4]$ and $[BiO_6]$ clusters produced by microwave irradiation are capable of decreasing the energetic barrier of the path connecting the two polymorphs.

(v) Based on the analysis of the geometry and electronic properties of the under-coordinated clusters (local coordination of P and Bi cations) appearing at the exposed surfaces of the morphology, we are capable to rationalize the mechanism of the photodegradation process of Rhodamine B under visible light irradiation.

Our findings elucidate the structural and electronic alterations along the phase transition between hexagonal and monoclinic phases of $BiPO_4$, which are induced by microwaves; further, these results serve as guidelines for engineers to optimize the structure and performance of future photocatalysts for environmental remediation applications.

REFERENCES

(1) Pan, C.; Zhu, Y. New Type of $BiPO_4$ Oxy-Acid Salt Photocatalyst with High Photocatalytic Activity on Degradation of Dye. Environ. Sci. Technol. **2010**, 44, 5570–5574.

(2) Lv, Y.; Zhu, Y.; Zhu, Y. Enhanced Photocatalytic Performance for the $BiPO_{4-x}$ Nanorod Induced by Surface Oxygen Vacancy. J. Phys. Chem. C **2013**, 117, 18520–18528.

(3) Krause-Rehberg, R.; Leipner, H. S. Positron Annihilation in Semiconductors: Defect Studies; Springer Science & Business Media, 1999.

(4) Wang, H.; Yuan, X.; Wu, Y.; Zeng, G.; Tu, W.; Sheng, C.; Deng, Y.; Chen, F.; Chew, J. W. Plasmonic Bi Nanoparticles and BiOCl Sheets as Cocatalyst Deposited on Perovskite-Type $ZnSn(OH)_6$ Microparticle with Facet-Oriented Polyhedron for Improved Visible-Light-Driven Photocatalysis. Appl. Catal. B Environ. **2017**, 209, 543–553.

(5) Fang, W.; Jiang, Z.; Yu, L.; Liu, H.; Shangguan, W.; Terashima, C.; Fujishima, A. Novel Dodecahedron $BiVO_4$:YVO_4 Solid Solution with Enhanced Charge Separation on Adjacent Exposed Facets for Highly Efficient Overall Water Splitting. J. Catal. **2017**, 352, 155–159.

(6) Liu, Y.; Lv, Y.; Zhu, Y.; Liu, D.; L. Zong, R.; Zhu, Y. Fluorine Mediated Photocatalytic Activity of $BiPO_4$. Appl. Catal. B-Environmental **2014**, 147, 851–857.

(7) Li, J.; Dong, X.; Sun, Y.; Cen, W.; Dong, F. Facet-Dependent Interfacial Charge Separation and Transfer in Plasmonic Photocatalysts. Appl. Catal. B Environ. **2018**, 226, 269–277.

(8) Wang, J.; Li, J.; Li, H.; Duan, S.; Meng, S.; Fu, X.; Chen, S. Crystal Phase-Controlled Synthesis of $BiPO_4$ and the Effect of Phase Structure on the Photocatalytic Degradation of Gaseous Benzene. Chem. Eng. J. **2017**, 330, 433–441.

(9) Pan, C.; Li, D.; Ma, X.; Chen, Y.; Zhu, Y. Effects of Distortion of PO_4 Tetrahedron on the Photocatalytic Performances of $BiPO_4$. Catal. Sci. Technol. **2011**, 1, 1399–1405.

(10) Achary, S. N.; Errandonea, D.; Muñoz, A.; Rodríguez-Hernández, P.; Manjón, F. J.; Krishna, P. S. R.; Patwe, S. J.; Grover, V.; Tyagi, A. K. Experimental and Theoretical Investigations on the Polymorphism and Metastability of $BiPO_4$. Dalt. Trans. **2013**, 42 (42), 14999-15015.

(11) Liu, Y.-F.; Ma, X.-G.; Yi, X.; Zhu, Y.-F. Controllable Synthesis and Photocatalytic Performance of Bismuth Phosphate Nanorods. Acta Physico-Chimica Sinica. **2012**, 28, 654–660.

(12) Xue, F.; Li, H.; Zhu, Y.; Xiong, S.; Zhang, X.; Wang, T.; Liang, X.; Qian, Y. Solvothermal Synthesis and Photoluminescence Properties of $BiPO_4$ Nano-Cocoons and Nanorods with Different Phases. J. Solid State Chem. **2009**, 182, 1396–1400.

(13) Li, G.; Ding, Y.; Zhang, Y.; Lu, Z.; Sun, H.; Chen, R. Microwave Synthesis of $BiPO_4$ Nanostructures and Their Morphology-Dependent Photocatalytic Performances. J. Colloid Interface Sci. **2011**, 363, 497–503.

(14) Geng, J.; Hou, W. H.; Lv, Y. N.; Zhu, J. J.; Chen, H. Y. One-Dimensional $BiPO_4$ Nanorods and Two-Dimensional BiOCl Lamellae: Fast Low-Temperature Sonochemical Synthesis, Characterization, and Growth Mechanism. Inorg. Chem. 2005, 44, 8503–8509.

(15) Pan, C; Xu, J.; Wang, Y.; Li, D.; Zhu, Y. Dramatic Activity of $C_3N_4/BiPO_4$ Photocatalyst with Core/Shell Structure Formed by Self-Assembly. Adv. Funct. Mater. **2012**, 22, 1518–1524.

(16) Guan, M.; Sun, J.; Tao, F.; Xu, Z. A Host Crystal for the Rare-Earth Ion Dopants: Synthesis of Pure and Ln-Doped Urchinlike $BiPO_4$ Structure and Its Photoluminescence. Cryst. Growth Des. **2008**, 8, 2694–2697.

(17) Zhang, Q.; Tian, H.; Li, N.; Chen, M.; Teng, F. Controllable Growth of Novel $BiPO_4$ Dendrites by an Innovative Approach and High Energy Facets-Dependent Photocatalytic Activity. CrystEngComm **2014**, 16, 8334–8339.

(18) Wu, Z.; Liu, J.; Tian, Q.; Wu, W. Efficient Visible Light Formaldehyde Oxidation with 2D P-n Heterostructure of $BiOBr/BiPO_4$ Nanosheets at Room Temperature. ACS Sustain. Chem. Eng. **2017**, 5, 5008–5017.

(19) Lv, H.; Guang, J.; Liu, Y.; Tang, H.; Zhang, P.; Lu, Y.; Wang, J. Synthesis of Ionic Liquid-Modified $BiPO_4$ Microspheres with Hierarchical Flower-like Architectures and Enhanced Photocatalytic Activity. RSC Adv. **2015**, 5, 100625–100632.

(20) Errandonea, D.; Gomis, O.; Santamaría-Perez, D.; García-Domene, B.; Muñoz, A.; Rodríguez-Hernández, P.; Achary, S. N.; Tyagi, A. K.; Popescu, C. Exploring the High-Pressure Behavior of the Three Known Polymorphs of $BiPO_4$: Discovery of a New Polymorph. J. Appl. Phys. **2015**, 117, 105902.

(21) Li, P.; Yuan, T.; Li, F.; Zhang, Y. Phosphate Ion-Driven $BiPO_4$:Eu Phase Transition. J. Phys. Chem. C **2019**, 123, 4424–4432.

(22) Naidu, B. S.; Vishwanadh, B.; Sudarsan, V.; Vatsa, R. K. $BiPO_4$: A Better Host for Doping Lanthanide Ions. Dalt. Trans. **2012**, 41, 3194–3203.

(23) Ding, C.; Han, A.; Ye, M.; Zhang, Y.; Yao, L.; Yang, J. Hydrothermal Synthesis and Characterization of Novel Yellow Pigments Based on V^{5+} Doped $BiPO_4$ with High Near-Infrared Reflectance. RSC Adv. **2018**, 8, 19690–19700.

(24) Lv, Y.; Liu, Y.; Zhu, Y.; Zhu, Y. Surface Oxygen Vacancy Induced Photocatalytic Performance Enhancement of a $BiPO_4$ Nanorod. J. Mater. Chem. A **2014**, 2, 1174–1182.

(25) Stuerga, D. Microwaves in Organic Synthesis; Hoz, A. D. L. H., Loupy, A., Eds.; Wiley-VCH Verlag GmbH & Co KGaA: Weinheim, Germany, 2012.

(26) Kappe, C. O.; Pieber, B.; Dallinger, D. Microwave Effects in Organic Synthesis: Myth or Reality? Angew. Chemie Int. Ed. **2013**, 52, 1088–1094.

(27) Kappe, C. O. How to Measure Reaction Temperature in Microwave-Heated Transformations. Chem. Soc. Rev. **2013**, 42, 4977–4990.

(28) Landry, C. C.; Lockwood, J.; Barron, A. R. Synthesis of Chalcopyrite Semiconductors and Their Solid Solutions by Microwave Irradiation. Chem. Mater. **1995**, 7, 699–706.

(29) Komarneni, S.; Katsuki, H. Nanophase Materials by a Novel Microwave-Hydrothermal Process. Pure App. Chem. **2002**, 74, 1537-1543.

(30) Macario, L. R.; Moreira, M. L.; Andrés, J.; Longo, E. An Efficient Microwave-Assisted Hydrothermal Synthesis of $BaZrO_3$ Microcrystals: Growth Mechanism and Photoluminescence Emissions. CrystEngComm **2010**, 12, 3612–3619.

(31) Polshettiwar, V.; Varma, R. S. Green Chemistry by Nano-Catalysis. Green Chem. **2010**, 12, 743–754.

(32) Bilecka, I.; Niederberger, M. Microwave Chemistry for Inorganic Nanomaterials Synthesis. Nanoscale **2010**, 2, 1358–1374.

(33) Pereira, P. F. S.; Gouveia, A. F.; Assis, M.; de Oliveira, R. C.; Pinatti, I. M.; Penha, M.; Gonçalves, R. F.; Gracia, L.; Andrés, J.; Longo, E. $ZnWO_4$ Nanocrystals: Synthesis, Morphology, Photoluminescence and Photocatalytic Properties. Phys. Chem. Chem. Phys. **2018**, 20, 1923–1937.

(34) Ebadi, M.; Mat-Teridi, M. A.; Sulaiman, M. Y.; Basirun, W. J.; Asim, N.; Ludin, N. A.; Ibrahim, M. A.; Sopian, K. Electrodeposited P-Type Co_3O_4 with High Photoelectrochemical Performance in Aqueous Medium. RSC Adv. **2015**, 5, 36820–36827.

(35) Stuerga, D. Microwave-Material Interactions and Dielectric Properties, Key Ingredients for Mastery of Chemical Microwave Processes. Microwaves in Organic Synthesis. Hoz, A. D. L. H., Loupy, A., Eds.; Wiley-VCH Verlag GmbH & Co KGaA: Weinheim, Germany, 2016.

(36) Xu, Y.; Ma, X.; Jisong, H.; Xu, A.; Wang, Z.; Huang, C. Structures and Energetics of Low-Index Stoichiometric $BiPO_4$ Surfaces. CrystEngComm **2019**, 21, 4730-4739.

(37) Zheng, X.; Wang, J.; Liu, J.; Wang, Z.; Chen, S.; Fu, X. Photocatalytic Degradation of Benzene over Different Morphology $BiPO_4$: Revealing the Significant Contribution of High–Energy Facets and Oxygen Vacancies. Appl. Catal. B Environ. **2019**, 243, 780–789.

(38) Lee, C.; Yang, W.; Parr, R. G. Development of the Colle-Salvetti Correlation-Energy Formula into a Functional of the Electron Density. Phys. Rev. B **1988**, 37, 785–789.

(39) Dovesi, R.; Orlando, R.; Erba, A.; Zicovich-Wilson, C. M.; Civalleri, B.; Casassa, S.; Maschio, L.; Ferrabone, M.; De La Pierre, M.; D'Arco, P.; et al. CRYSTAL14: A Program for the Ab Initio Investigation of Crystalline Solids. Int. J. Quantum Chem. **2014**, 114, 1287–1317.

(40) Heifets, E.; Kotomin, E. A.; Bagaturyants, A. A.; Maier, J. Ab Initio Study of $BiFeO_3$: Thermodynamic Stability Conditions. J. Phys. Chem. Lett. **2015**, 6, 2847–2851.

(41) Peintinger, M. F.; Oliveira, D. V.; Bredow, T. Consistent Gaussian Basis Sets of Triple-Zeta Valence with Polarization Quality for Solid-State Calculations. J. Comput. Chem. **2013**, 34, 451–459.

(42) Monkhorst, H. J.; Pack, J. D. Special Points for Brillouin-Zone Integrations. Phys. Rev. B **1976**, 13, 5188–5192.

(43) Barmparis, G. D.; Lodziana, Z.; Lopez, N.; Remediakis, I. N. Nanoparticle Shapes by Using Wulff Constructions and First-Principles Calculations. Beilstein J. Nanotechnol. **2015**, 6, 361–368.

(44) Wulff G. Z. XXV. Zur Frage der Geschwindigkeit des Wachsthums und der Auflösung der Krystallflächen. Zeitschrift für Kristallographie. **1901**, 34, 449-530.

(45) Andrés, J.; Gracia, L.; Gouveia, A. F.; Ferrer, M. M.; Longo, E. Effects of Surface Stability on the Morphological Transformation of Metals and Metal Oxides as Investigated by First-Principles Calculations. Nanotechnology **2015**, 26, 405703.

(46) Fabbro, M. T.; Saliby, C.; Rios, L. R.; La Porta, F. A.; Gracia, L.; Li, M. S.; Andrés, J.; Santos, L. P. S.; Longo, E. Identifying and Rationalizing the Morphological, Structural, and Optical Properties of β-Ag_2MoO_4 Microcrystals, and the Formation Process of Ag Nanoparticles on Their Surfaces: Combining Experimental Data and First-Principles Calculations. Sci. Technol. Adv. Mater. **2015**, 16, 65002.

(47) Bomio, M. R. D.; Tranquilin, R. L.; Motta, F. V; Paskocimas, C. A.; Nascimento, R. M.; Gracia, L.; Andres, J.; Longo, E. Toward Understanding the Photocatalytic Activity of $PbMoO_4$ Powders with Predominant (111), (100), (011), and (110) Facets. A Combined Experimental and Theoretical Study. J. Phys. Chem. C **2013**, 117, 21382–21395.

(48) Lu, J. J.; Ulrich, J. The Influence of Supersaturation on Crystal Morphology – Experimental and Theoretical Study. Cryst. Res. Technol. **2005**, 40, 839–846.

(49) Longo, V. M.; Gracia, L.; Stroppa, D. G.; Cavalcante, L. S.; Orlandi, M.; Ramirez, A. J.; Leite, E. R.; Andrés, J.; Beltrán, A.; Varela, J. A.; et al. A Joint Experimental and Theoretical Study on the Nanomorphology of $CaWO_4$ Crystals. J. Phys. Chem. C **2011**, 115, 20113–20119.

(50) Botelho, G.; Andres, J.; Gracia, L.; Matos, L. S.; Longo, E. Photoluminescence and Photocatalytic Properties of Ag_3PO_4 Microcrystals: An Experimental and Theoretical Investigation. Chempluschem **2016**, 81, 202–212.

(51) Oliveira, M. C.; Gracia, L.; Nogueira, I. C.; Carmo Gurgel, M. F. do; Mercury, J. M. R.; Longo, E.; Andrés, J. Synthesis and Morphological Transformation of $BaWO_4$ Crystals: Experimental and Theoretical Insights. Ceram. Int. **2016**, 42, 10913–10921.

(52) Silva, G. S.; Gracia, L.; Fabbro, M. T.; Serejo dos Santos, L. P.; Beltrán-Mir, H.; Cordoncillo, E.; Longo, E.; Andrés, J. Theoretical and Experimental Insight on Ag2CrO4 Microcrystals: Synthesis, Characterization, and Photoluminescence Properties. Inorg. Chem. 2016, 55 (17), 8961–8970. https://doi.org/10.1021/acs.inorgchem.6b01452.

(53) Gouveia, A. F.; Ferrer, M. M.; Sambrano, J. R.; Andrés, J.; Longo, E. Modeling the Atomic-Scale Structure, Stability, and Morphological Transformations in the Tetragonal Phase of $LaVO_4$. Chem. Phys. Lett. **2016**, 660, 87–92.

(54) Gao, Z.; Sun, W.; Hu, Y.; Liu, X. Anisotropic Surface Broken Bond Properties and Wettability of Calcite and Fluorite Crystals. Trans. Nonferrous Met. Soc. China **2012**, 22, 1203–1208.

(55) Gao, Z.; Fan, R.; Ralston, J.; Sun, W.; Hu, Y. Surface Broken Bonds: An Efficient Way to Assess the Surface Behaviour of Fluorite. Miner. Eng. **2019**, 130, 15–23.

(56) Ferrer, M. M.; Gouveia, A. F.; Gracia, L.; Longo, E.; Andrés, J. A 3D Platform for the Morphology Modulation of Materials: First Principles Calculations on the Thermodynamic Stability and Surface Structure of Metal Oxides: Co_3O_4, α-Fe_2O_3, and In_2O_3. Model. Simul. Mater. Sci. Eng. **2016**, 24, 25007.

(57) Macedo, N. G.; Gouveia, A. F.; Roca, R. A.; Assis, M.; Gracia, L.; Andrés, J.; Leite, E. R.; Longo, E. Surfactant-Mediated Morphology and Photocatalytic Activity of α-Ag_2WO_4 Material. J. Phys. Chem. C **2018**, 122, 8667–8679.

(58) Romero, B.; Bruque, S.; Aranda, M. A. G.; Iglesias, J. E. Syntheses, Crystal Structures, and Characterization of Bismuth Phosphates. Inorg. Chem. **1994**, 33, 1869–1874.

(59) Zhu, L.; Ma, X.-G.; Wei, Y.; Chu, L.; Wang, H.-H.; Huang, C.-Y. Origin of Photocatalytic Activity of $BiPO_4$: The First-Principles Calculations. Jiegou Huaxue **2017**, 36, 1299–1306.

(60) Darkwah, W. K.; Adormaa, B. B.; Sandrine, M. K. C.; Ao, Y. Modification Strategies for Enhancing the Visible Light Responsive Photocatalytic Activity of the $BiPO_4$ Nano-Based Composite Photocatalysts. Catal. Sci. Technol. **2019**, 9, 546–566.

(61) Gao, H.; Zheng, C.; Yang, H.; Niu, X.; Wang, S. Construction of a CQDs/Ag_3PO_4/$BiPO_4$ Heterostructure Photocatalyst with Enhanced Photocatalytic Degradation of Rhodamine B under Simulated Solar Irradiation. Micromachines . **2019**, 10, 557.

(62) Aguilar-Reynosa, A.; Romaní, A.; Ma. Rodríguez-Jasso, R.; Aguilar, C. N.; Garrote, G.; Ruiz, H. A. Microwave Heating Processing as Alternative of Pretreatment in Second-Generation Biorefinery: An Overview. Energy Convers. Manag. **2017**, 136, 50–65.

(63) Errandonea, D.; Gomis, O.; Rodriguez-Hernández, P.; Muñoz, A.; Ruiz-Fuertes, J.; Gupta, M.; Achary, S. N.; Hirsch, A.; Manjon, F. J.; Peters, L.; et al. High-Pressure Structural and Vibrational Properties of Monazite-Type $BiPO_4$, $LaPO_4$, $CePO_4$, and $PrPO_4$. J. Phys. Condens. Matter. **2018**, 30, 65401.

(64) Lakshminarayana, G.; Dao, T. D.; Chen, K.; Sharma, M.; Takeda, T.; Brik, M. G.; Kityk, I. V.; Singh, S.; Nagao, T. Effect of Different Surfactants on Structural and Optical Properties of Ce^{3+} and Tb^{3+} Co-Doped $BiPO_4$ Nanostructures. Opt. Mater. (Amst). **2015**, 39, 110–117.

(65) Li, J.; Yuan, H.; Zhu, Z. First-Principles Energy Band Calculation and One Step Synthesis of N-Doped $BiPO_4$. J. Alloys Compd. **2015**, 640, 290-297.

(66) Pan, C.; Zhu, Y. A Review of BiPO4{,} a Highly Efficient Oxyacid-Type Photocatalyst{,} Used for Environmental Applications. Catal. Sci. Technol. 2015, 5 (6), 3071–3083.

(67) Milanez, J.; de Figueiredo, A. T.; de Lazaro, S.; Longo, V. M.; Erlo, R.; Mastelaro, V. R.; Franco, R. W. A.; Longo, E.; Varela, J. A. The Role of Oxygen Vacancy in the Photoluminescence Property at Room Temperature of the $CaTiO_3$. J. Appl. Phys. 2009, 106 (4), 43526.

(68) Longo, V. M.; Cavalcante, L. S.; de Figueiredo, A. T.; Santos, L. P. S.; Longo, E.; Varela, J. A.; Sambrano, J. R.; Paskocimas, C. A.; De Vicente, F. S.; Hernandes, A. C. Highly Intense Violet-Blue Light Emission at Room Temperature in Structurally Disordered $SrZrO_3$ Powders. Appl. Phys. Lett. **2007**, 90, 91906.

(69) Gracia, L.; Longo, V. M.; Cavalcante, L. S.; Beltrán, A.; Avansi, W.; Li, M. S.; Mastelaro, V. R.; Varela, J. A.; Longo, E.; Andrés, J. Presence of Excited Electronic State in $CaWO_4$ Crystals Provoked by a Tetrahedral Distortion: An Experimental and Theoretical Investigation. J. Appl. Phys. **2011**, 110, 43501.

(70) Anicete-Santos, M.; Orhan, E.; de Maurera, M. A.; Simões, L. G. P.; Souza, A. G.; Pizani, P. S.; Leite, E. R.; Varela, J. A.; Andrés, J.; Beltrán, A.; et al. Contribution of Structural Order-Disorder to the Green Photoluminescence of $PbWO_4$. Phys. Rev. B **2007**, 75, 165105.

(71) Stearns, E.I. (1988), Commission Internationale de L'Éclairage, Colorimetry, 2nd ed., Publication CIE No. 15.2, 78; Central Bureau of the CIE, Vienna, 1987. Gaithersburg, Maryland 20899. Color Res. Appl., 13: 64-65.

(72) Tongay, S.; Suh, J.; Ataca, C.; Fan, W.; Luce, A.; Kang, J. S.; Liu, J.; Ko, C.; Raghunathanan, R.; Zhou, J.; et al. Defects Activated Photoluminescence in Two-Dimensional Semiconductors: Interplay between Bound, Charged, and Free Excitons. Sci. Rep. **2013**, 3, 2657.

(73) Gupta, S. K.; Sudarshan, K.; Ghosh, P. S.; Srivastava, A. P.; Bevara, S.; Pujari, P. K.; Kadam, R. M. Role of Various Defects in the Photoluminescence Characteristics of Nanocrystalline $Nd_2Zr_2O_7$: An Investigation through Spectroscopic and DFT Calculations. J. Mater. Chem. C **2016**, 4, 4988–5000.

(74) Wu, Z.; Zhao, W.; Jiang, J.; Zheng, T.; You, Y.; Lu, J.; Ni, Z. Defect Activated Photoluminescence in WSe_2 Monolayer. J. Phys. Chem. C **2017**, 121, 12294–12299.

(75) Longo, V. M.; de Figueiredo, A. T.; de Lázaro, S.; Gurgel, M. F.; Costa, M. G. S.; Paiva-Santos, C. O.; Varela, J. A.; Longo, E.; Mastelaro, V. R.; DE Vicente, F. S.; et al. Structural Conditions That Leads to Photoluminescence Emission in $SrTiO_3$: An Experimental and Theoretical Approach. J. Appl. Phys. **2008**, 104, 23515.

(76) Silva Junior, E.; La Porta, F. A.; Liu, M. S.; Andrés, J.; Varela, J. A.; Longo, E. A Relationship between Structural and Electronic Order–Disorder Effects and Optical Properties in Crystalline TiO_2 Nanomaterials. Dalt. Trans. **2015**, 44, 3159–3175.

(77) Klein, P. B.; Nwagwu, U.; Edgar, J. H.; Freitas, J. A. Photoluminescence Investigation of the Indirect Band Gap and Shallow Impurities in Icosahedral $B_{12}As_2$. J. Appl. Phys. **2012**, 112, 13508.

(78) Hizhnyi, Y. A.; Nedilko, S. G.; Chornii, V. P.; Slobodyanik, M. S.; Zatovsky, I. V; Terebilenko, K. V. Electronic Structures and Origin of Intrinsic Luminescence in Bi-Containing Oxide Crystals $BiPO_4$, $K_3Bi_5(PO_4)_6$, $K_2Bi(PO_4)(MoO_4)$, $K_2Bi(PO_4)(WO_4)$ and $K_5Bi(MoO_4)_4$. J. Alloys Compd. **2014**, 614, 420–435.

(79) Liu, B.; Zhao, X.; Terashima, C.; Fujishima, A.; Nakata, K. Thermodynamic and Kinetic Analysis of Heterogeneous Photocatalysis for Semiconductor Systems. Phys. Chem. Chem. Phys. **2014**, 16, 8751–8760.

(80) Kumar, K. V.; Porkodi, K.; Rocha, F. Langmuir–Hinshelwood Kinetics – A Theoretical Study. Catal. Commun. **2008**, 9, 82–84.

(81) Kröger, F. A.; Vink, H. J. Relations between the Concentrations of Imperfections in Solids. J. Phys. Chem. Solids **1958**, 5, 208–223.

(82) Barrios Trench, A.; Machado, T.; Fernandes Gouveia, A.; Assis, M.; Trindade, L.; Santos, C.; Perrin, A.; Christiane, P.; Oliva, M.; Andres, J.; et al. Connecting Structural, Optical, and Electronic Properties and Photocatalytic Activity of Ag_3PO4 :Mo Complemented by DFT Calculations. Appl. Catal. B Environ. **2018**, 238, 198-211

FIGURES

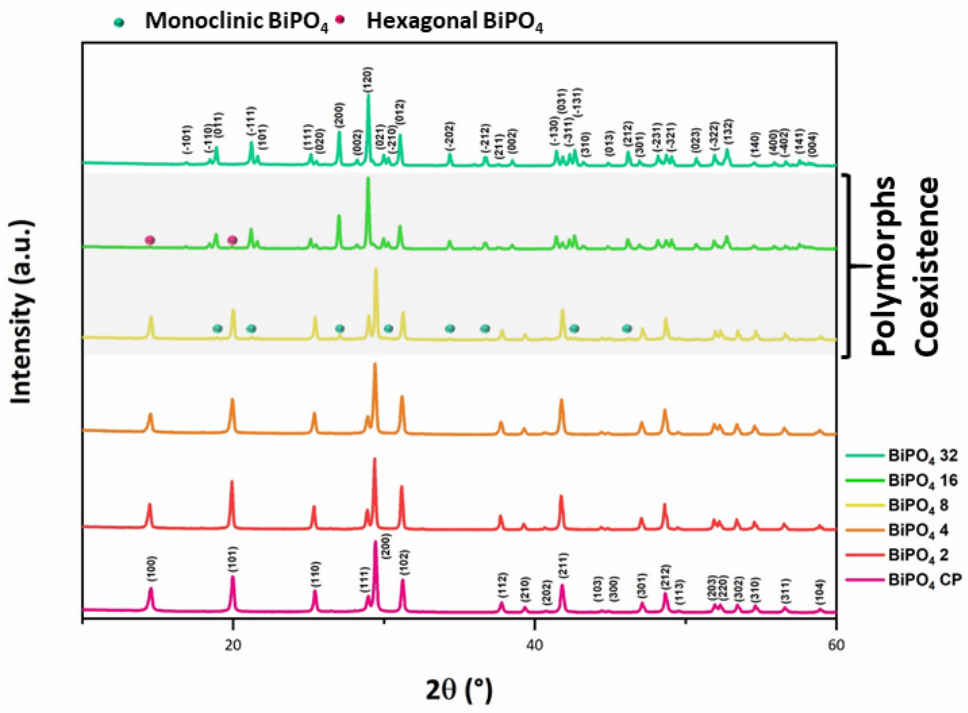

Figure 1. XRD of $BiPO_4$ powders obtained by CP and microwave irradiation at different times.

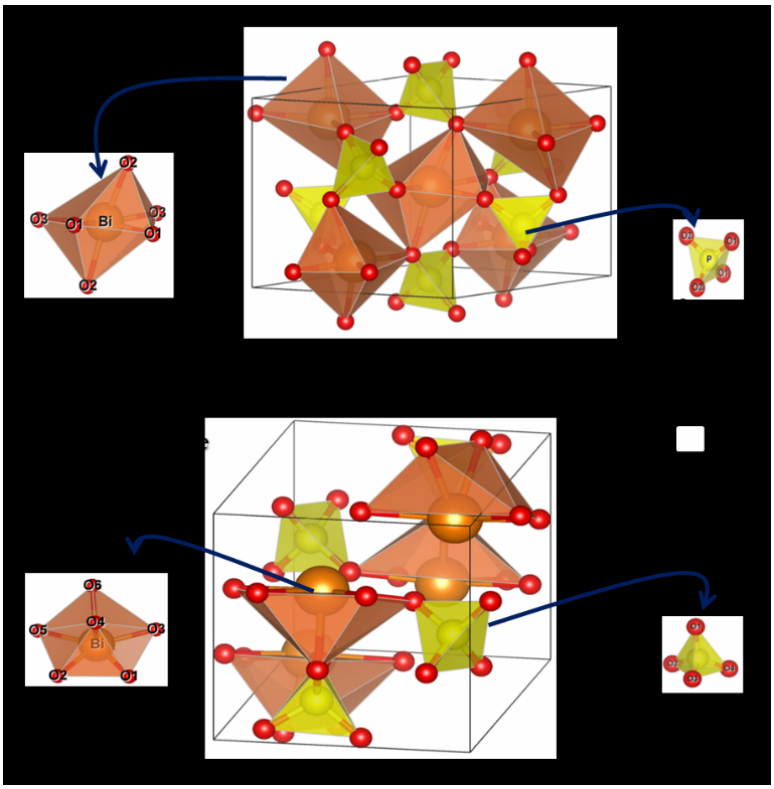

Figure 2. A 3D representation of hexagonal and monoclinic $BiPO_4$ structures. The $[BiO_6]$ and $[PO_4]$ clusters, as building blocks of these materials, are displayed.

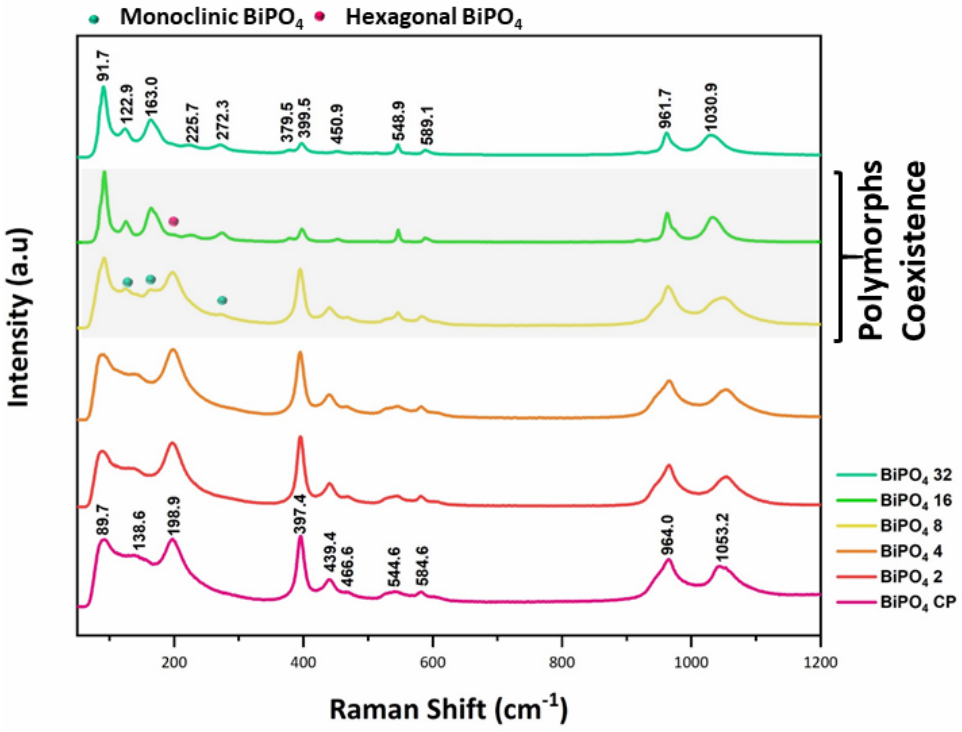

Figure 3. Micro-Raman spectra of $BiPO_4$ powders obtained by CP and under microwave irradiation at different times.

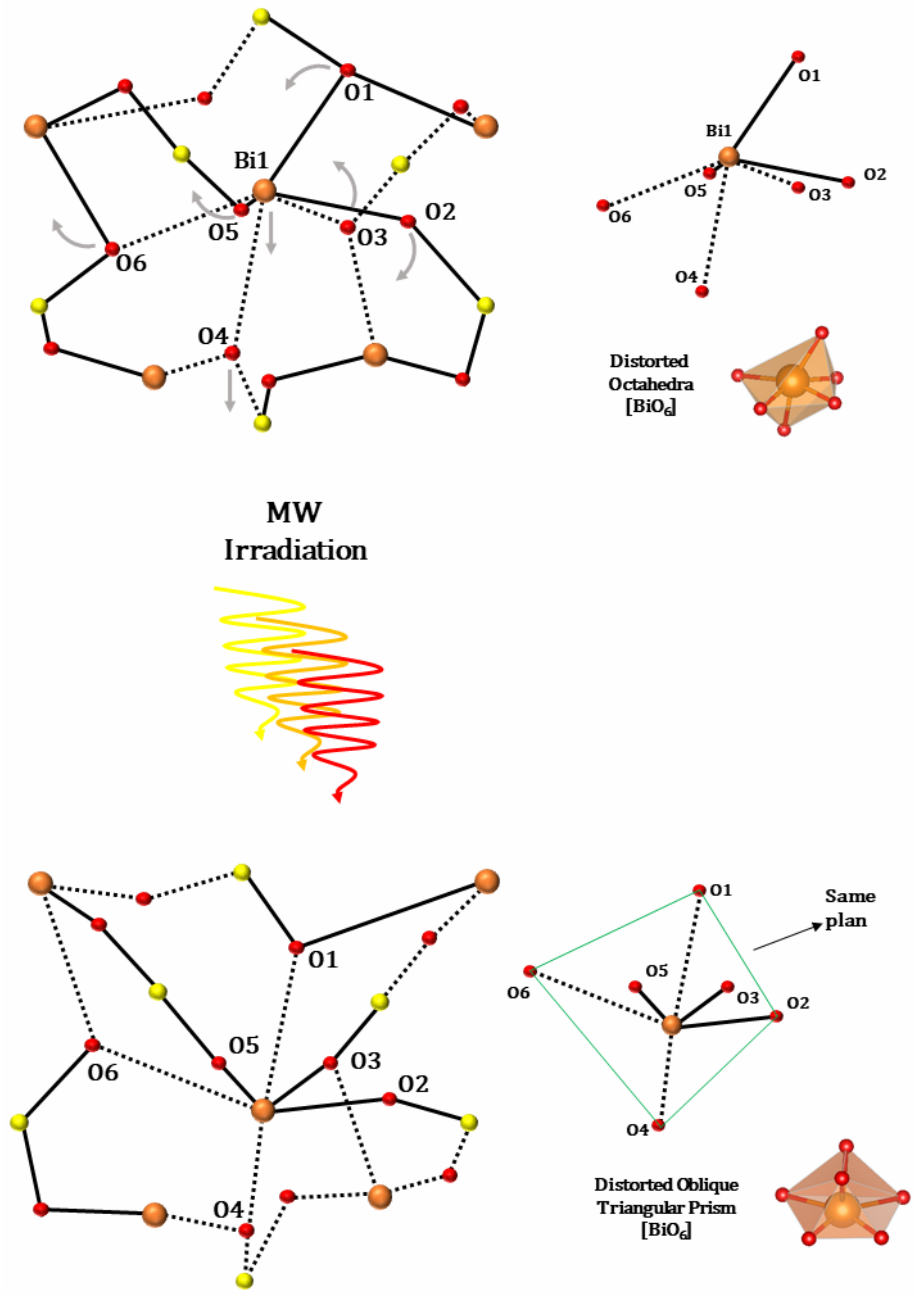

Figure 4. Representation of the vibration mode located at 70.67 cm^{-1}, associated to the rotation of the O anions at $[BiO_6]$ that are responsible to the phase transition from the hexagonal (distorted octahedra $[BiO_6]$) to monoclinic (distorted oblique triangular prism $[BiO_6]$) polymorph of $BiPO_4$ under microwave irradiation.

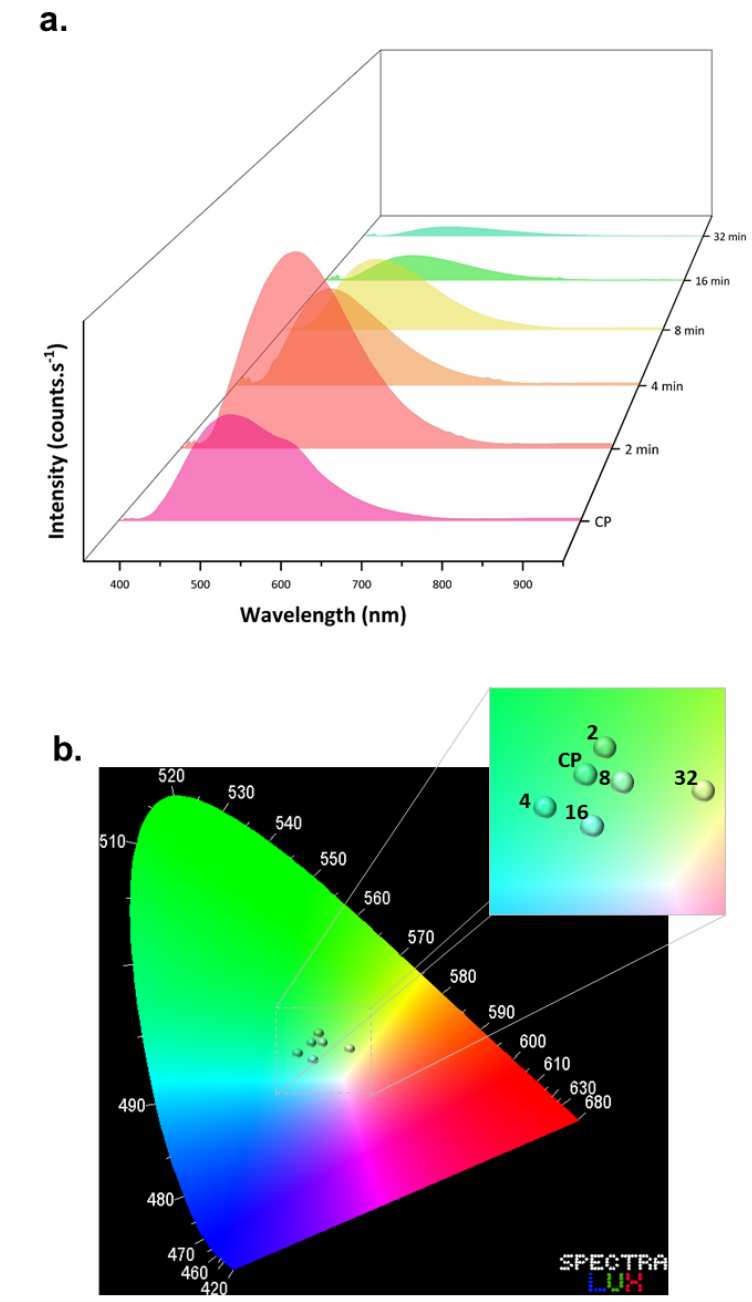

Figure 5. PL spectra of $BiPO_4$ powders obtained by CP method and posterior microwave irradiation at different times and **b.** *Commission International de l'Eclairage* (CIE) chromaticity coordinates for the samples obtained by SpectraLux software.

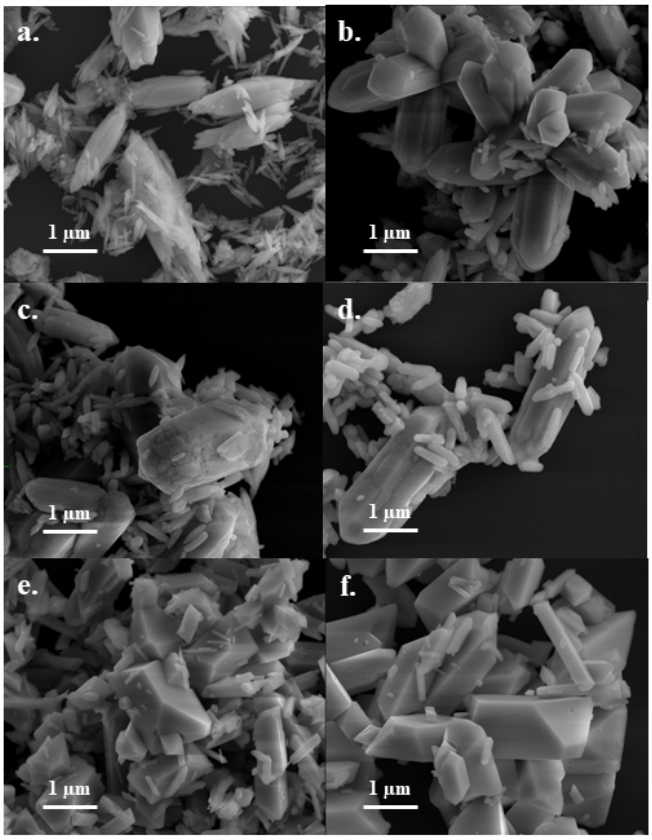

Figure 6. SEM images of $BiPO_4$ powders obtained by **a.** CP and at **b.** 2, **c.** 4, **d.** 8, **e.** 16 and **f.** 32 min of microwave irradiation.

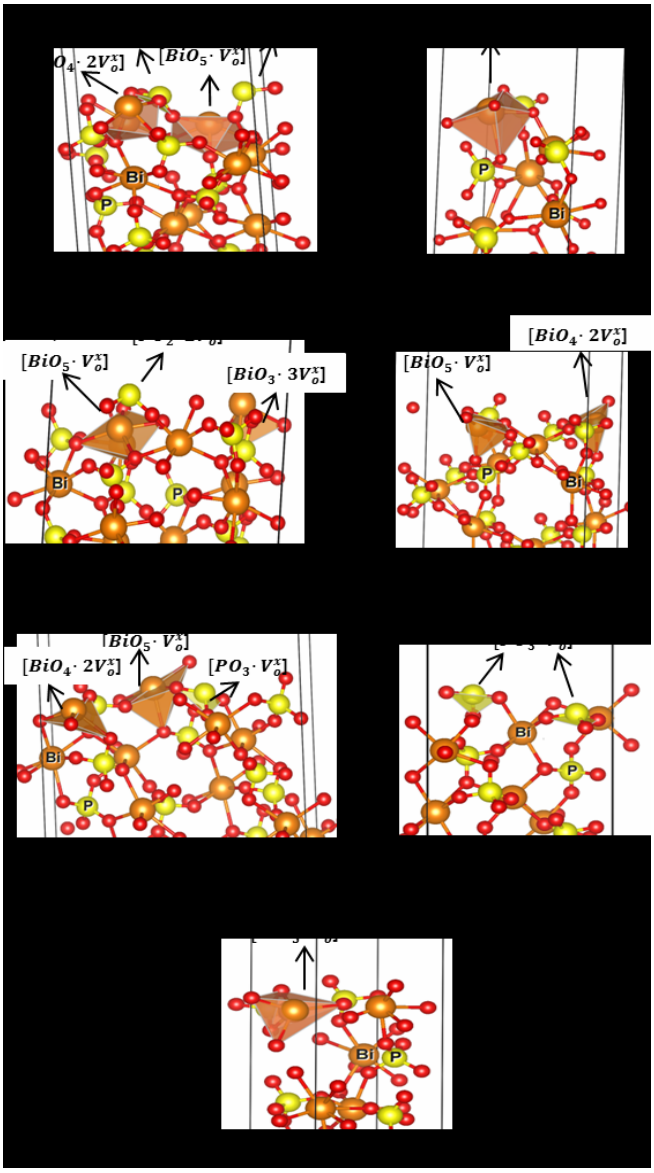

Figure 7. Surface models , , ,, , , and of hexagonal $BiPO_4$. Bi, P, and O atoms are represented by orange, yellow, and red balls, respectively. The under-coordination clusters for Bi and P presents at top of each surface are also displayed. The vacancies of oxygen are indicated using the Kröger-Vink notation.

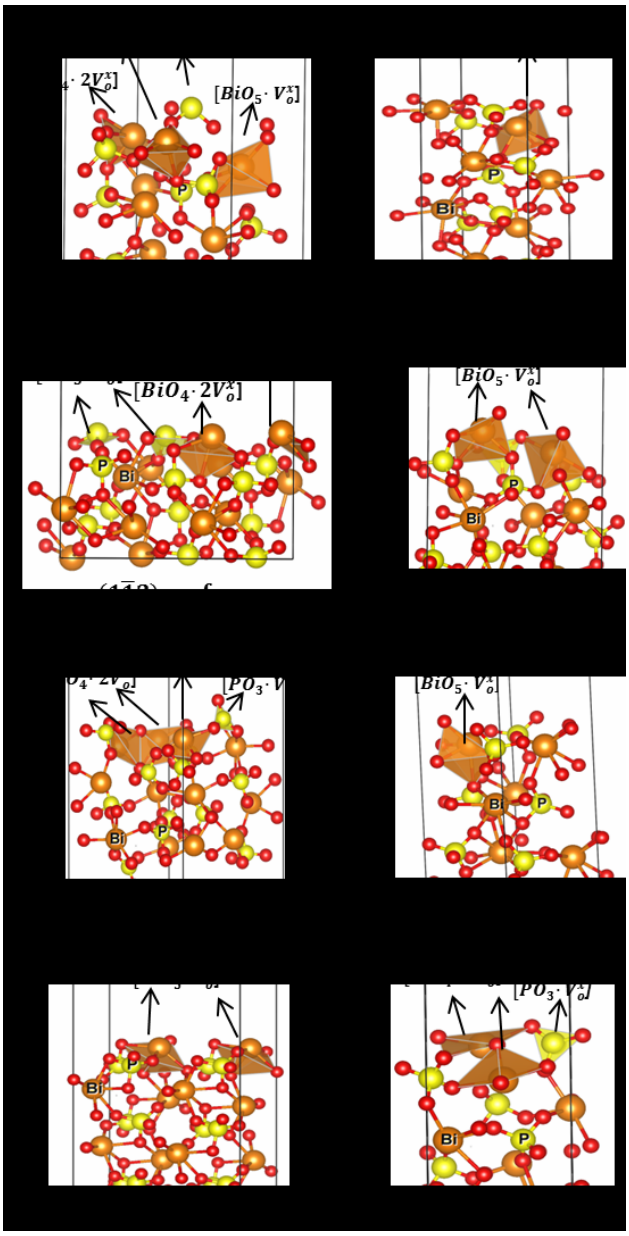

Figure 8. Surface models (, , ,, , , and of monoclinic $BiPO_4$. Bi, P, and O atoms are represented by orange, yellow, and red balls, respectively. The under-coordination clusters for Bi and P presents at top of each surface are also displayed. The vacancies of oxygen are indicated using the Kröger-Vink notation.

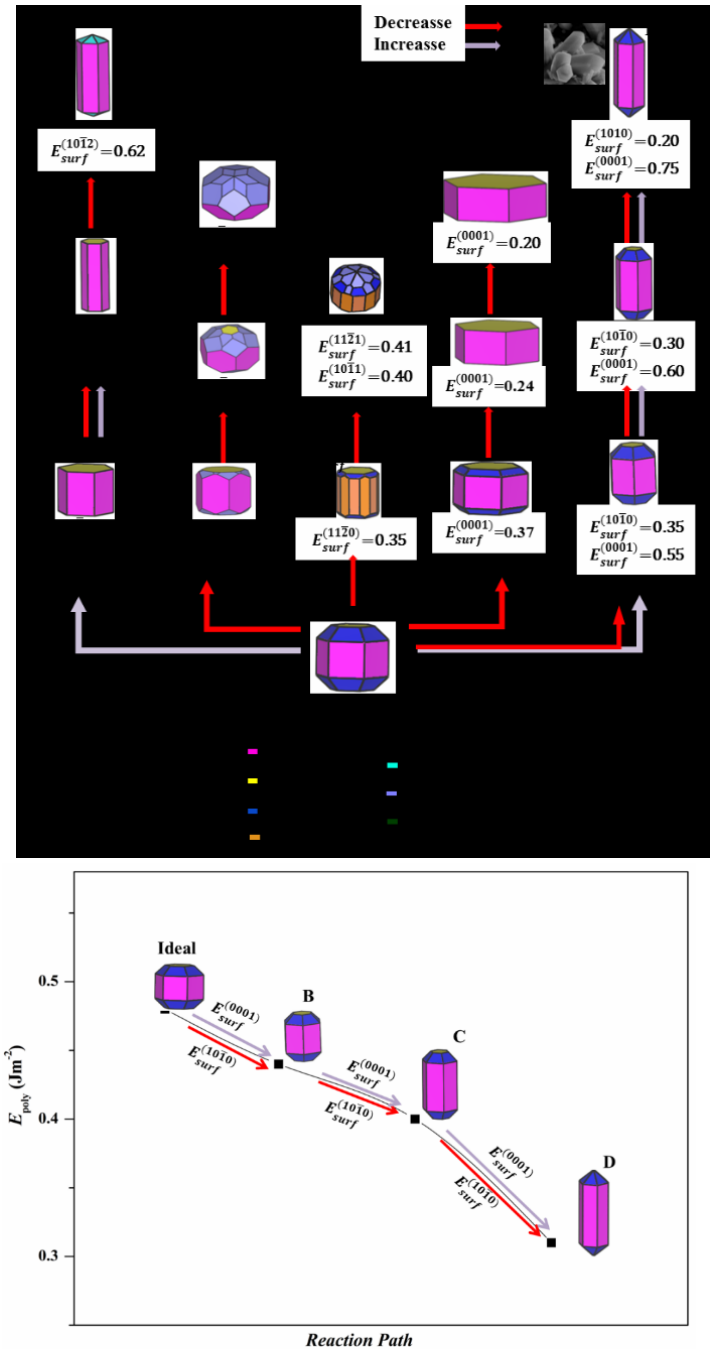

Figure 9. Available morphologies of hexagonal $BiPO_4$ obtained by the Wulff construction considering the , , ,, , , and surfaces (top). Experimental SEM image is also included for comparison purposes. Energy profile connecting the ideal and experimental morphology (bottom). in Jm^{-2}.

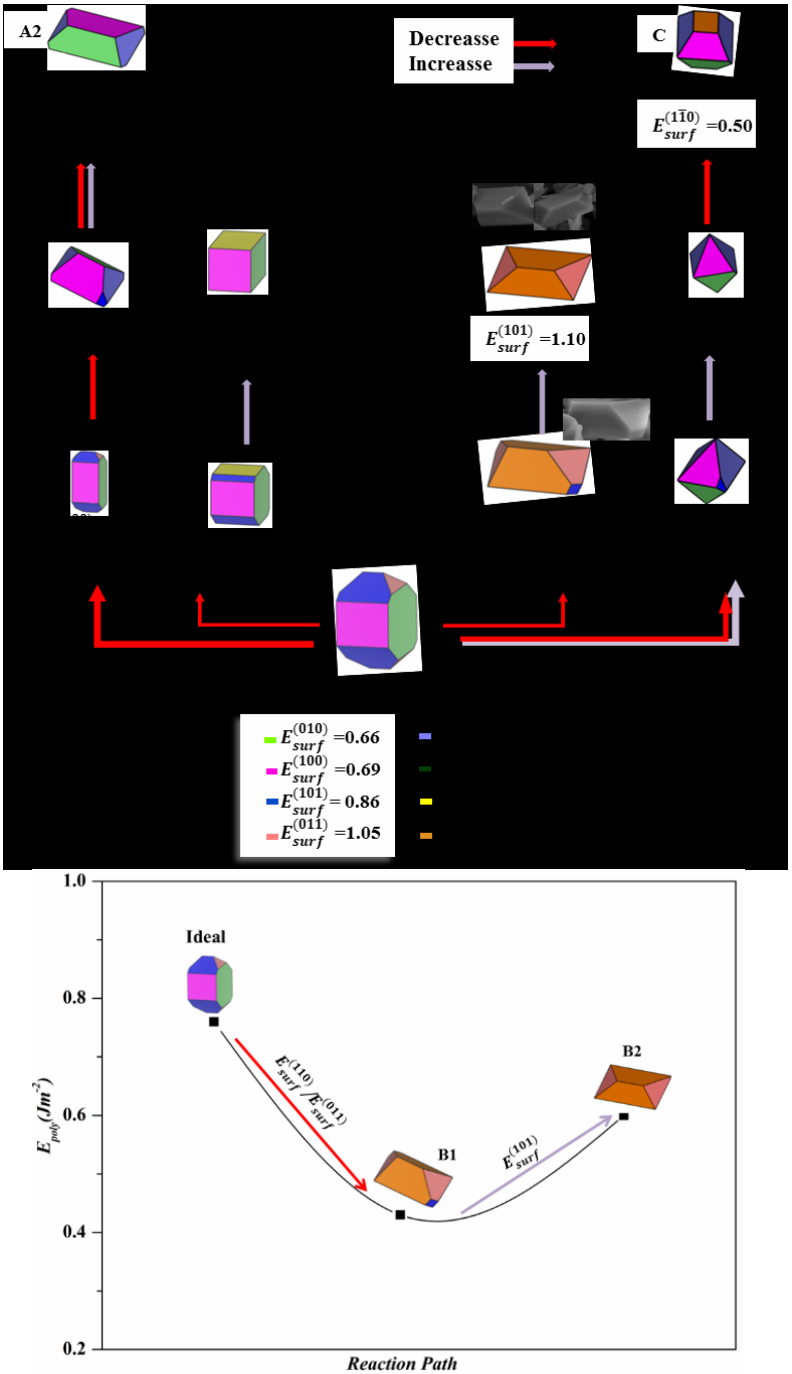

Figure 10. Available morphologies of monoclinic $BiPO_4$ obtained by the Wulff construction considering the , ,, , , , and surfaces (top) Experimental SEM images are also included for comparison purposes. Energy profile connecting the ideal and experimental morphology (bottom). in Jm^{-2}.

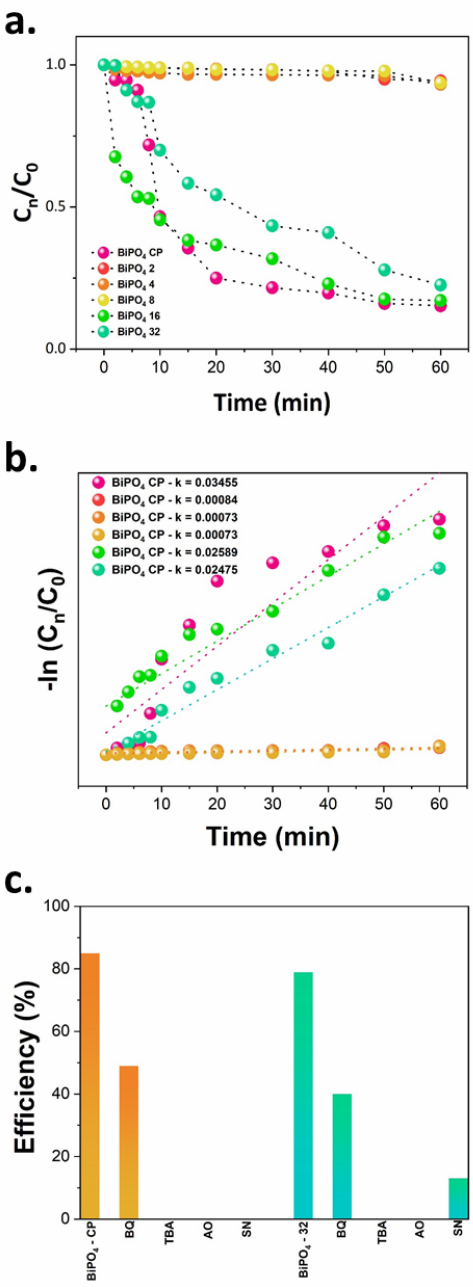

Figure 11. a. Relative concentration of RhB dye (C_n/C_0), **b.** reaction kinetics of RhB degradation $-\ln(C_n/C_0)$ versus time (min) for of $BiPO_4$ powders and **c.** efficiency of degradation (%) of RhB dye under exposure to UV-vis radiation, in the presence of different scavengers for the $BiPO_4$ CP and the $BiPO_4$ irradiated by microwaves for 32 min.

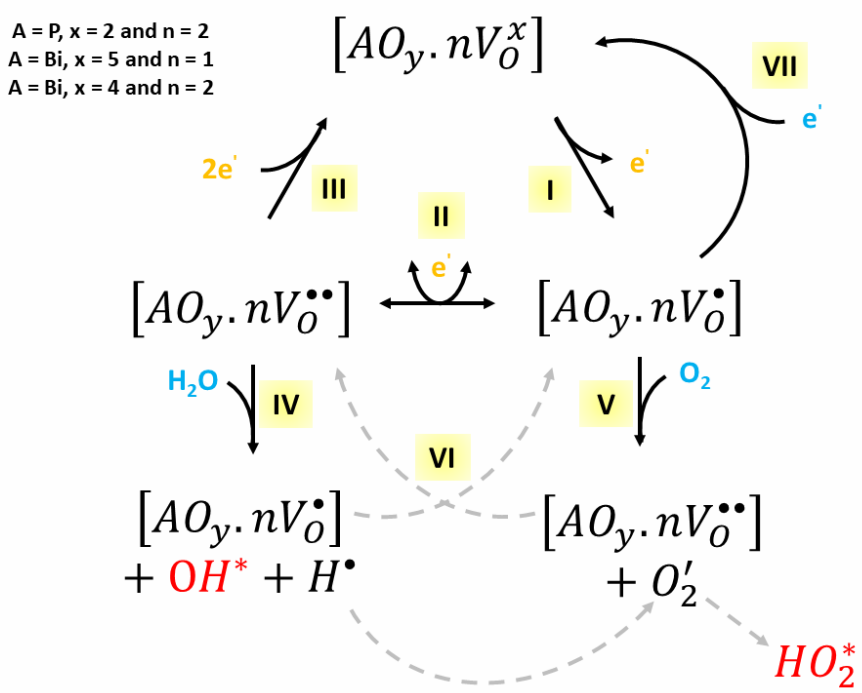

Figure 12. Mechanism for the generation of the reactive oxygen species of the $BiPO_4$ samples.

ASSOCIATED CONTENT

Supporting Information (PDF)

AUTHOR INFORMATION

Corresponding Author

*elson.liec@gmail.com

Author Contributions

The manuscript was written through contributions of all authors. All authors have given approval to the final version of the manuscript. †‡§¥£¤These authors contributed equally.

ACKNOWLEDGMENT

This work was funded in part by Fundação de Amparo à Pesquisa do Estado de São Paulo - FAPESP (2013/07296-2), FINEP, Conselho Nacional de Desenvolvimento Cientifico e Tecnológico - CNPq (166281/2017-4) and CAPES. J.A. acknowledges Universitat Jaume I for project UJI-B2016-25, Generalitat Valenciana for project PrometeoII/2014/022, ACOMP/2014/270, and ACOMP/2015/1202, and Ministerio de Economia y Competitividad (Spain) project CTQ2015-65207-P and Ministerio de Ciencia, Innovación y Universidades (Spain) project PGC2018-094417-B-I00 for supporting this research financially.

TOC

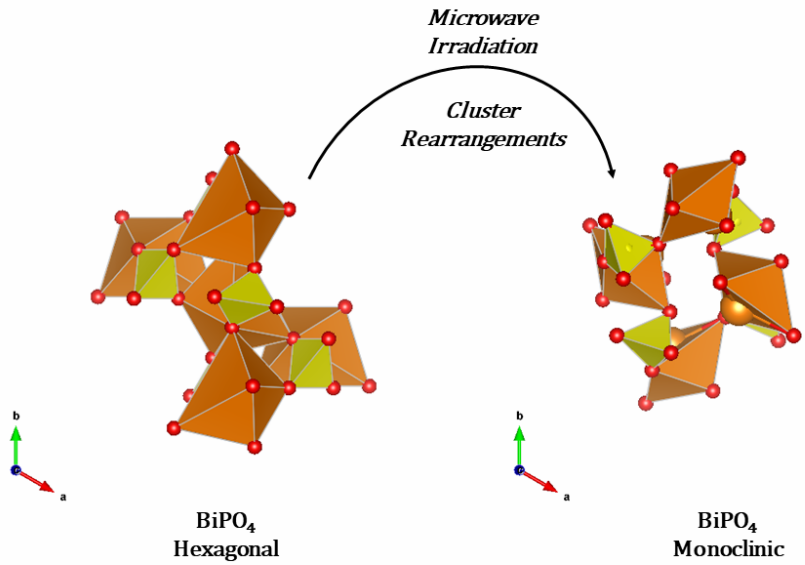

Synopsis: Through microwave irradiation, morphological changes in $BiPO_4$ are observed which are directly connected with its Rhodamine B photodegradation activity. Furthermore, according to the variation of the irradiation time, the conversion of the hexagonal phase obtained to monoclinic occurs. Theoretical simulations of the surfaces of the different phases show us the dependence of the vacancies of the superficial clusters for photodegradation, thus, explaining the variation of this property